Freie Universität Berlin

Understanding the redox behavior of transition metal complexes: from molecular models to proteins

Dissertation zur Erlangung des akademischen Grades des
Doktors der Naturwissenschaften (Dr. rer. nat.)

eingereicht im Fachbereich Biologie, Chemie, Pharmazie
der Freien Universität Berlin

vorgelegt von

Ana Patricia L Gámiz-Hernández

aus Mexiko

Berlin, August 2010

Dedication

This work is dedicated

to the memory of my mother Mariana Hernández,

to my father Fernando Gámiz who has always supported me,

to my sisters Norma and Leticia,

to my brothers Eduardo, Jorge, Hector and Oscar,

to the memory of my friend Felipe.

Acknowledgments

- I would like to thank my supervisor Prof. Dr. E. W. Knapp, for overseeing my work as a Master and Ph.D. student and for guiding me into the field of Biophysics. I really admire his broad expertise and longstanding experience that combines Physics, Biochemistry and Chemistry. I am deeply thankful for his useful advice and because he guided me into challenging and interesting projects that I consider will help me considerably in the future.

- Support for this work was provided by a grant from CONACyT (Consejo Nacional para la Ciencia y la Tecnologia) from the Mexican Council of Science and with the supervision of the DAAD (Deutscher Akademischer Austausch Dienst). I am grateful for the recommendation and support given by the researchers in Mexico: Prof. Ruben Santamaria Ortiz and Prof. Maria Ester Brandan from the Physics Institute (UNAM).

- This research was partially supported by the SFB498 (Sondernforschungsbereich 498) with the project "Protein-Cofactor Interactions in Biological Processes". I am really thankful to all members for their support and useful discussions during seminars and workshops.

- I would like to thank Prof. Dr. H. H. Limbach that allowed me to take part in the "Dahlem International Postgraduate School of Chemistry" and encouraged me to participate in the "Hydrogen Bonding and Hydrogen Transfer" seminars, symposia and training.

- I am also very grateful to Gernot Kieseritzky, developer of Karlsberg$^+$ who kindly adapted his program for my computations and participated in useful discussions.

- I wish to thank to Dr. A. Galstyan for introducing me to quantum chemical methods for computing absolute redox potentials and for useful discussions.

- During my Ph. D. work, the AG Knapp members took care of keeping the computer network running, installed and maintained many useful programs. They helped me in many discussions during the coffee break and the group seminars and created a nice working atmosphere. I am very glad to have the chance to have worked with them, in particular with Dawid Rasinski, Jorge Numata, Dr. Alok Juneja and Dr. M. El-Amine Madjet.

- Finally, I would like to thank Dr. F. Bettella with who I had many interesting and constructive discussions that improved the quality of my work.

Die vorliegende Arbeit wurde unter Anleitung von Prof. Dr. E. W. Knapp am Institut für Chemie/Kristallographie der Freien Universität Berlin im Fachbereich Biologie, Chemie und Pharmazie durchgeführt.

1. Gutachter: Prof. Dr. E. Walter Knapp, Freie Universität Berlin

2. Gutachter: Prof. Dr. Wolfram Saenger, Freie Universität Berlin

Tag der Disputation: 13.09.2010

Preamble

This cumulative thesis summarizing my research work consist of three parts. The first part covers electrostatic studies on iron-sulfur model compounds. The first peer reviewed publication, belonging to this part, focuses on the influence of hydrogen bonds on iron-sulfur complexes, Chapter 2. The computation of Rubredoxin (Rd) redox potentials is reported in Chapter 3. The research paper summarizing the results on Rd at the time of submission of the thesis is in preparation and is not considered as a peer reviewed publication. The third part addresses protein modeling and redox potential computations of an artificial cytochrome b of unknow structure, Chapter 4. The results of the last part are presented in the second peer-review published journal.

Statutory Declaration

I hereby testify that this thesis is the result of my own work and research, except of the references given in the bibliography. This work contains material that is the copyright property of others, which cannot be reproduced without the permission of the copyright owner.

Ana Patricia Gamiz-Hernandez

List of publications

- **Understanding rubredoxin redox potentials: role of H-bonds on model complexes**
  Ana P. Gamiz-Hernandez, Artur S. Galstyan, Ernst W. Knapp
  J. Chem. Theory Comput. **2009**, 5, 2898-2908.
  http://pubs.acs.org/doi/abs/10.1021/ct900328c

- **Understanding properties of cofactors in proteins: redox potentials of synthetic cytochrome b**
  Ana P. Gamiz-Hernandez, Gernot Kieseritzky, Artur S. Galstyan, Ozgur Demir-Kavuk, Ernst W. Knapp
  ChemPhysChem **2010**, 11, 1196-1206.
  http://www3.interscience.wiley.com/journal/123362544/abstract

- **Rubredoxin function: redox behavior from electrostatics**
  Ana P. Gamiz-Hernandez, G. Kiesertizky, H. Ishikita, E. W. Knapp
  This article is in preparation and is presented in Chapter 3 of this Thesis. The article is not available online.

Contents

Chapter 1

Introduction

Contents

1.1 Electron transfer in metalloproteins

Electron transfer (ET) reactions represent an essential mechanism in the metabolism of all living cells participating in a large variety of anabolic and catabolic processes. Transition metal complexes are found at the active sites of a large variety of redox-active proteins due to their ability of existing in more than one stable oxidation state rendering them to function in catalysis, detoxification, transport and storage in biological processes [1]. The processes catalyzed by such proteins can require the transfer of both electrons and protons to a substrate in the direct neighborhood of the metal complex, or can simply involve the transfer of an electron between proteins (i.e. as part of an electron transfer chain such as those involved in respiration or photosynthesis). Due to the physiological importance of electron transfer metalloproteins, there has been much effort devoted to understanding their electrochemical properties.

The redox potentials of electrons transfer proteins vary over a wide range, even when the type of redox center is the same [2]. There is no single factor that determines the reduction potentials of redox-active proteins but rather they are affected by different contributions. The key factors influencing redox potentials are the contributions to the Gibbs energy difference between the two redox states, resulting from bonding interactions at the redox center, electrostatic interactions between the redox- center charge and polar groups within the protein and solvent, and redox-state dependent conformational changes. The relative importance of these factors is likely to vary from protein to protein [2].

Major types of electron transfer proteins are cytochromes and iron-sulfur proteins, may posess several electron transfer chains like in photosynthesis or respiration.

1.2 Iron-sulfur proteins

Iron-sulfur complexes (ISC) are common redox-active cofactors in proteins mediating electron transfer processes such as in photosynthesis, catalysis and respiration. Iron-sulfur proteins (ISP) are ubiquitous in nature, and they expand the redox potential in a large interval from $-700\,mV$ to $+400\,mV$ (see Fig. 1.1).

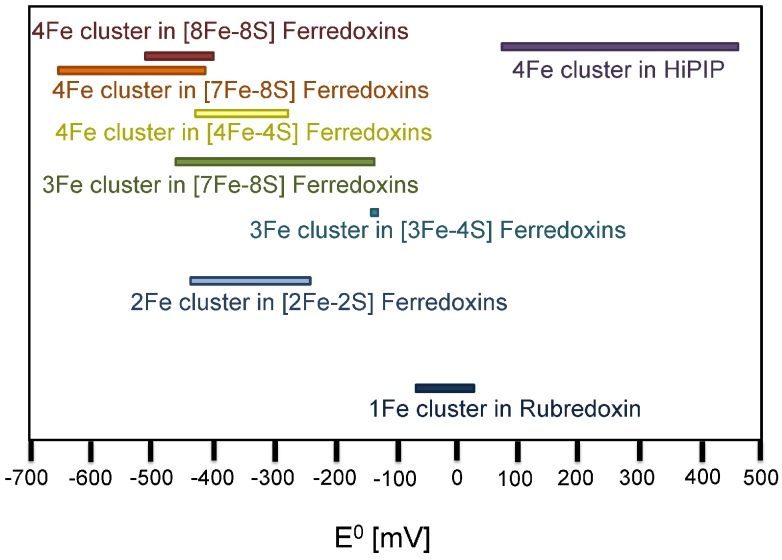

Figure 1.1: **Range of redox potentials observed for iron sulfur proteins [relative to the standard hydrogen electrode (SHE)] adapted from reference [3, 4].**

There are a wide range of different iron-sulfur electron transfer proteins, which vary in the number of iron centers, Fig. 1.1. There are different iron-sulfur structures observed, for example: $Fe(cys)_4$, $Fe_2S_2(cys)_4$, $Fe_2S_2(cys)_2(his)_2$, $Fe_3S_4(cys)_3$, $Fe_4S_4(cys)_4$ and $Fe_4S_4(cys)_3(his)$. Since iron can readily exist in the $+3$ or $+2$ charge states, the following oxidation states are available for the Fe_xS_y cluster core: $+2$, $+1$, 0 (Fe_2S_2); $+1$, 0, -1 (Fe_3S_4); $+4$, $+3$, $+2$, $+1$, 0 (Fe_4S_4). However, an iron sulfur cluster in a protein typically only exhibits one redox process when studied by cyclic voltammetry. The term ferredoxin (Fd) is used to describe Fe_2S_2, Fe_3S_4 and Fe_4S_4 clusters, whereas FeS proteins are referred to rubredoxins (Rds).

Structural analyses of iron-sulfur proteins have shown that there is little variation in the structure of the iron-sulfur clusters of a given type in different proteins. Therefore, the wide variation in measured redox potentials has been attributed to variations in the cluster environment within the protein (e. g., hydrogen bonding, electrostatic interactions, solvent accessibility, and hydrophobicity) [5–8].

Iron-sulfur proteins play essential roles in living organisms and according to their function they can be divided in electron transfer chains (Rd, Fd and Rieske proteins), catalysis (oxidoreductases), Photosynthesis (Fd and Rieske proteins), Respiratory chain (Rieske proteins) and Nitrogen fixation (Fds).

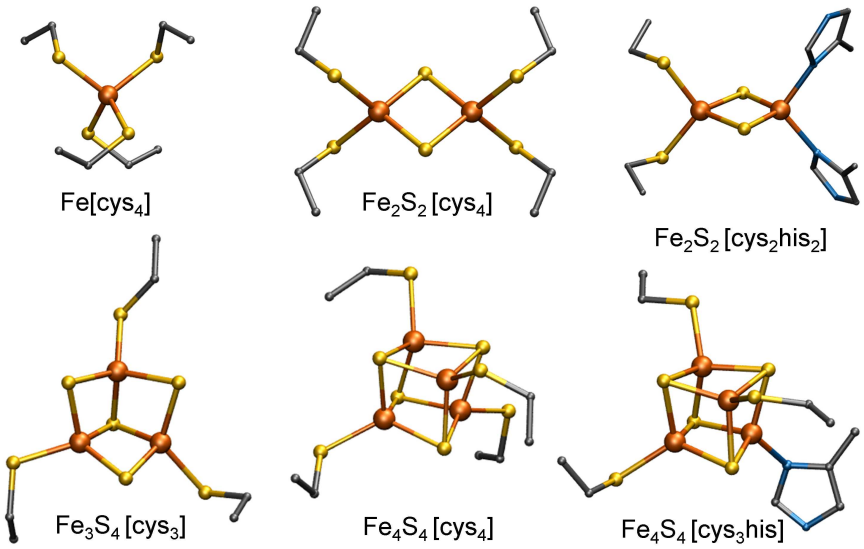

Figure 1.2: **Molecular structures of iron sulfur prosthetic groups found in iron-sulfur proteins. On top from left to right: the mono-iron cluster from rubredoxin (Rd), the two iron ferredoxin (Fd) and the two iron-clusters from Rieske proteins; the latter is ligated to two histidines instead of two cysteine residues as in Fd. On the bottom, the three iron ferredoxin with three cysteine ligands (left), the four iron-ferredoxin with four cysteine ligands (middle) and the four iron-ferredoxin with three cysteine and one histidine ligands (right).**

1.3 Model compounds of iron-sulfur proteins

One method that has been used for examining the effect of protein structural variations on redox potentials has been the study of model compounds; that is, small molecular complexes that contain some of the features of the active site under investigation. It should be stressed that model compounds cannot reproduce exactly the complex environment inside a protein, they are used for systematic variations of specific structural features.

In the case of iron-sulfur proteins, one interesting approach is to consider the simplest iron-sulfur model complex containing just one iron coordinated to four cysteine like ligands, (Fe[cys_4], Fig. 1.2. This model avoids problems of antiferromagnetic coupling arising in multi-core transition metal iron-sulfur cluster, Fig. 1.2. The energetics of redox states were computed for a Rd model depicted in Fig. 1.3 (A), and several other iron-sulfur complex (ISC) models with different features, like different number and type of H-bonds within the ISC and larger models whose chemical compositions are more analogous to the relevant part of the ISC in Rd, Fig. 1.3 (B) [8].The contributions of the hydrogen bonds on the shift of the ISC redox potentials are in agreement with experimental values measured in other types of iron-sulfur proteins [6, 9] as presented in Chapter 2.

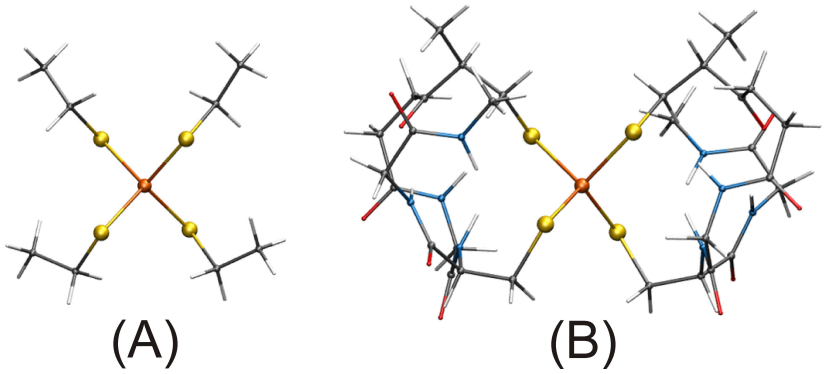

Figure 1.3: **Model compounds of Rd using two levels of modeling (A) just the iron with ligands that corresponds the side chains of the ligand cysteine residues and (B) the iron sulfur center with the amide H-bonds formed with the backbone of six residues. Taken from reference [8].**

1.4 Rubredoxin

The Rd-like models introduced in the previous section are quite useful to understand the factors that affect the ISC redox potential inside the protein. These factors are the ISC conformation adopted inside the protein, the number and type of H-bonds toward the ISC and the dielectric environment given by the surrounding amino acids and the solvent accessibility. Nevertheless, when placing the ISC inside the protein, other factors may as well shift the redox potential like conformational changes upon reduction and protonation states of the different titratable residues. Therefore, computations of ISC redox potentials in proteins should describe all these factors. In Chapter 3 we present an investigation of several factors that contribute to the shift of redox potentials in Rds. Agreement of computed and measured values is achieved (RMSD of 16 mV) by considering geometry relaxation of hydrogen atoms, amino acid side chains surrounding the ISC and salt-bridges in crystal structures of Rds from different species and mutants.

1.5 Cytochromes

Cytochromes are part of a larger group of proteins in which a heme prosthetic group is the active site. The oxidized heme group consists of iron (III) coordinated to a porphyrin ring system. Cytochrome **b** (Cb) is one of the most studied cytochromes and consists of a heme **b** (Fig. 1.4) with two axial histidine ligands belonging to two alpha-helices.

Cytochrome **b** belongs to a major class of protein complexes including cytochrome $\mathbf{bc}_1$ and cytochrome $\mathbf{b}_6\mathbf{f}$. Cytochrome $\mathbf{bc}_1$ (Cbc_1) is one of the four major membrane protein complexes of the respiratory system residing in the inner mitochondrial membrane, Fig. 1.5. In this figure, the Cbc_1 complex consist of four redox centers, namely, two heme groups, b_H and b_L, of cytochrome **b**, one heme group

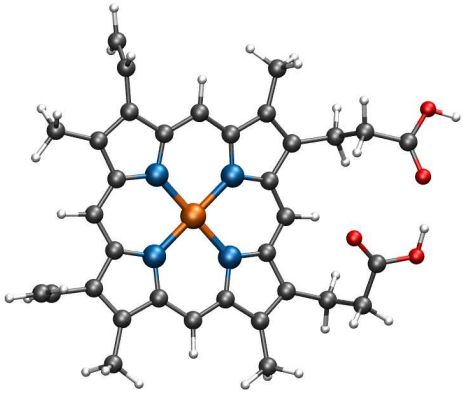

Figure 1.4: **Heme b of cytochrome b consisting of one iron in the center coordinated to a porphyrin group. In cytochrome b the iron is ligated by two histidine residues from two parallel α- helices. In the figure, the two propionic groups $COOH$ are oriented to the right. The protonation state of this two acidic groups is coupled with the redox state of the iron.**

in cytochrome c_1, and one iron-sulfur cluster $[2Fe2S]$ of the Rieske protein. This complex transfers the electrons from ubiquinol to cytochrome **c** and uses the energy thus released to form an electrochemical gradient across the inner membrane.

The redox potential of heme **b** in the **Cb** proteins exhibit a range of redox potential values from $-200\,mV$ to $100\,mV$ [1] and it is readily adjusted by several factors: the protonation state of the heme propionates, the orientation of the heme-ligating histidine residues relative to the porphyrin plane and propionate groups, specific interactions of the heme group with polar and charged groups of the protein, and the protein dielectric environment in the heme neighbourhood. A major focus of the studies on cytochromes has been a mutational approach changing specific amino acid residues around the heme in order to investigate the effect of a particular residue on the structure and function of the protein.

This is the approach that we used to investigate the properties of heme **b** inside a protein [11] and it is explained in Chapter 4. Based on 399 artificial cytochrome **b** (**aCb**) models synthesized in the group of Haehnel [12] with available redox potentials, we generated the atomic coordinates for 31 **aCb** mutants that cover the whole interval of available redox potentials ranging from -148 to +89 mV. The crystal structures for these proteins are unknown, therefore the structures were modeled from scratch and their structures remain stable after energy minimization and molecular dynamics. This study allowed us to investigate the relation between structure and function of this type of proteins and elucidate some factors important to explain the differences in redox potential arising in the **aCb** mutants.

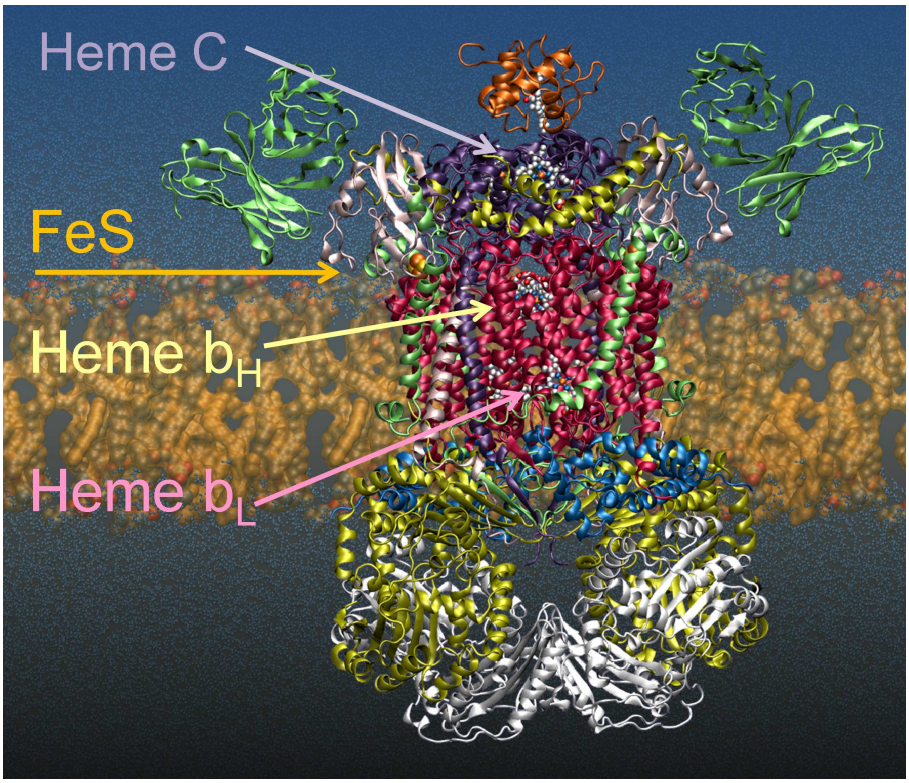

Figure 1.5: X-ray structure of the complex III: cytochrome $\mathbf{bc}_1$ n the respiratory electron transport chain from bovine heart (solved by Iwata et al., [10]. Cytochrome **b** is displayed in magenta in the middle indicating the two cofactors: heme $\mathbf{b}_H$ and heme $\mathbf{b}_L$ that are practically contained in a four-helix bundle. The Rieske iron-sulfur cluster (FeS) is indicated with an orange arrow. Cytochrome **c** is on the upper surface whose protein is depicted in violet colour.

1.6 Electrostatic computations of proteins

Understanding the way proteins control the redox potential of their cofactors is a problem of fundamental and practical importance. Such understanding should help in gaining a quantitative description of the way proteins control the specificity and efficiency of key biological processes. Even after elucidating the X-ray structure of redox proteins, explanation of the factors that determine the magnitude of their redox potentials remain unclear. Several factors have been proposed including conformational, dynamical, entropic and electrostatic, being the last one of great importance as the redox process involves a change in the charge of the redox cofactor.

Correlating the structure and function of biological molecules requires the knowledge of the corresponding relation between structure and energy. Probably the most important factors in such a structure-energy correlation are associated with electrostatic interactions [13–16]. Thus, a key requirement for a quantitative understanding of the action of redox-active biological molecules is the ability to correlate electrostatic interactions with structural information.

The study of electrostatic in macromolecules has progressed significantly in recent years [13–15] after it became more widely recognized that electrostatic potentials can be predicted quantitatively [14, 15, 17–24]. These predictions are based on approximations for solvated proteins. In these models, the electrostatic potential is obtained from a quantum chemical calculation of small molecules that have equivalent chemical groups, assigning partial unit charges to each atom, the so called "atomic partial charges".

One of the approaches to solve the protein electrostatic interactions is the continuum approach, where the protein is represented as dielectric continuum with a low dielectric constant and individual atomic partial charges, while the solvent is represented with a high dielectric constant without individual charges. By solving the Poisson-Boltzmann equation, this model provides a macroscopic description of electrostatic interactions of the solvent with a dissolved protein, whereas the protein is still represented in atomic detail.

These macroscopic electrostatic models have been used to determine the protonation and redox equilibria in proteins [15, 17, 25, 26]. A similar approach is used to compute the redox potentials of heme in cytochrome **b** presented in Chapter 4.

Recently, a new approach to compute the electrostatic energies with pH-dependent conformational relaxation of salt-bridges and H-bonds inside the protein was developed [24, 27]. These conformations are created by "self-consistent" geometry optimization of the input crystal structures combined with random changes of side chains of basic and acidic residues involved in salt-bridges and their neighbor residues. This strategy was also applied to compute redox potentials of Rd proteins but instead of pH-dependent conformations, redox adapted conformations are generated at ambient pH. The study is presented in Chapter 3.

Additionally, we present a short description of the theoretical methods applied to study molecular model complexes and proteins. These are continuum electrostatic theory based on the solution of the linearized Poisson-Boltzmann equation (Appendix A) to compute the energetics of titratable and redox active groups in a protein and the computation of redox potentials of iron-sulfur model compounds using a quantum chemical approach (Appendix B).

Chapter 2

Understanding rubredoxin redox potentials: role of H-bonds on model complexes

Ana P. Gamiz-Hernandez, Artur. S. Galstyan and E. Walter Knapp
J. Chem. Theory Comput. **2009**, 5, 2898-2908.
http://pubs.acs.org/doi/abs/10.1021/ct900328c

Contents

2.1 Contributions

- Modeling of Rubredoxin iron-sulfur complexes and computation of absolute redox potentials.
- Modeling of iron-sulfur complexes with different number of $S\cdots H-N$ and $S\cdots H-O$ H-bonds and computation of absolute redox potentials.
- Modeling of Rubredoxin like model with six amide H-bonds and computation of redox potential.
- Investigation and discussion about factors contributing to the computation of redox potential of iron-sulfur proteins.

2.2 Summary and discussion

The energetics of redox states in different models of rubredoxin-like iron-sulfur complexes (ISC) were computed using a combination of density functional and electrostatic continuum approach. In agreement with experiment, the calculated redox potential for the small ISC model $[Fe(SCH_2CH_3)_4]^{-1,-2}$ in acetonitrile was $-813\ mV$ [28] as compared to the measured value of $-838\ mV$ [29]. Surprisingly the experimental values for rubredoxin (Rd) are much higher ranging between -87

and $+39\ mV$. These large variations in redox potentials of ISC models and ISC in Rd are in part due to specific conformational symmetries adopted by the ligands due to both, the protein environment and type and number of H-bonds, and the dielectric environment, (Figure 2.1). In a dielectric environment corresponding to proteins ($\varepsilon = 20$), the computed ISC redox potentials shift positive by about $64\ mV$ for $Fe-S\cdots H-N$ and $95\ mV$ for $Fe-S\cdots H-O$ H-bonds, correlating well with data estimated from experiments on ISC proteins. In aqueous solutions ($\varepsilon = 80$), a positive shift of $58\ mV$ was computed for $Fe-S\cdots H-O$ H-bonds (using a model with the same ISC conformation as in Rd) in agreement with a measured value for Rd with partially solvent exposed ISC. The latter demonstrates the dependence of the ISC redox potentials on the environment (solvent or protein). For a model whose chemical composition is analogous to the relevant part of the ISC in a specific Rd, the computed redox potential of the model agrees with the measured value in Rd. This study allows to understand redox potential shifts for small ISC models and ISC in proteins [11]. A short explanation of continuum electrostatics and the method used to compute redox potentials of transition metal complexes is presented in Appendix A and B.

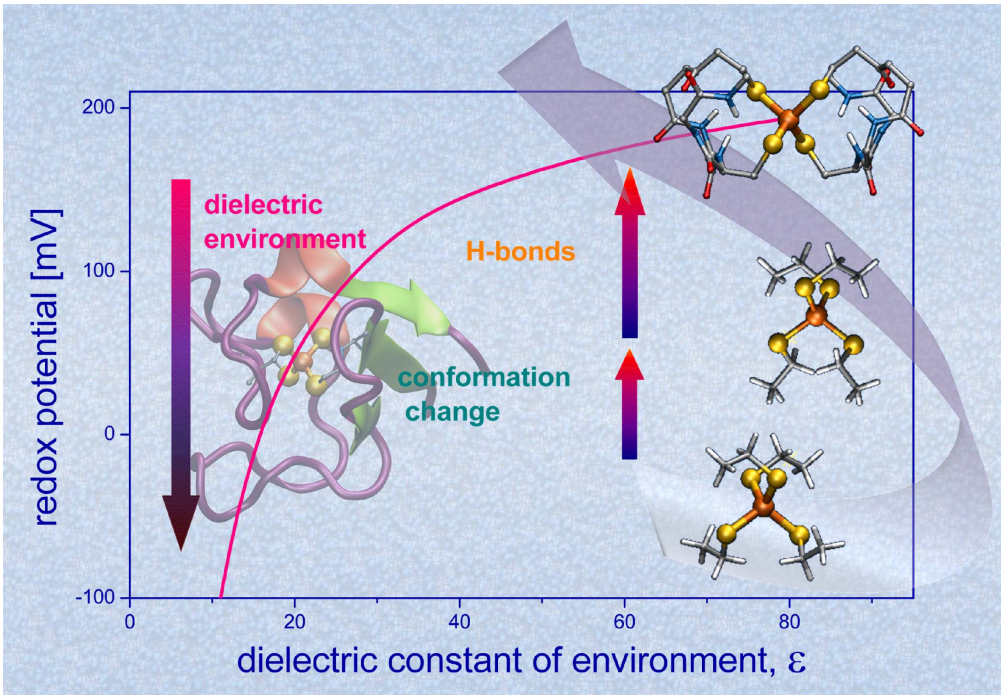

Figure 2.1: **Factors influencing the redox potential of rubredoxin models and differences due to changes in dielectric environment, water ($\varepsilon = 80$) and protein ($\varepsilon = 20$). The conformational change of a small iron-sulfur complex shifts positively the redox potential ($71\ mV$) (from S_4 to C_2 symmetry). Formation of H-bonds with sulfur shifts as well positively ($60-90\ mV$) the redox potential; a negative shift ($-200\ mV$) occurs moving from high to low dielectric environment (from water to protein).**

Chapter 3

Redox potentials in Rubredoxin

Contents

3.1 Summary

Continuum electrostatic theory was applied to compute redox potentials of rubredoxin (Rd) proteins. We used the multiple side chain conformers of the crystal structures and optimized hydrogen atom positions and geometries of salt-bridges self-consistently for given solvent pH and redox potential to obtain several global redox adapted conformers (RACs), which were used for electrostatic energy computations. Agreement with measured Rd redox potentials was obtained by Boltzmann averaging over these RACs. The following contributions to Rd redox potentials were discussed: side chain conformations, H-bond geometries of the iron-sulfur complex (ISC), dielectric environment defined by the Rd structure, composition of charged residues and salt-bridges. We considered Rds with available crystal structures from eight different species/strains of wild type (WT) and seven mutant Rds making up a total of 15 Rds for which we obtained a root mean square deviation (RMSD) of measured and computed Rd redox potentials of 16 mV. For the Rds from *Clostridium*

pasterianum (*Cp*) we considered 15 mutants (including WT *Cp*) where measured redox potentials are available. We used only the WT *Cp* structure to model the mutant structures without modifying the backbone. Hence, the geometry of the amide H-bonds with the ISC did not vary. Nevertheless, we obtained an RMSD of only 14 mV demonstrating that these H-bonds cannot be the only factor determining the Rd redox potentials. The full contribution of a single amide H-bond to the Rd redox potential was computed on average to be 63 mV, in agreement with *ab initio* computations on ISC models and experimental estimates for other iron sulfur proteins [6, 8]. Varying the amide H-bond length by 0.1 Å we obtained a change in Rd redox potential of about 13 mV. We analyzed the factors determining the Rd redox potentials of the mesophilic Rd from *Cp* and the thermophilic Rd from *Pyrococcus furiosus* (*Pf*). We found that half of the difference in redox potentials is due to sequence and half is due to backbone variations. In the sequence contribution half of the redox potential difference is due to different composition of charged residues. Albeit salt-bridge networks vary considerably between the two Rds, their influences seem to be compensated, such that they have no significant influence on the redox potential difference.

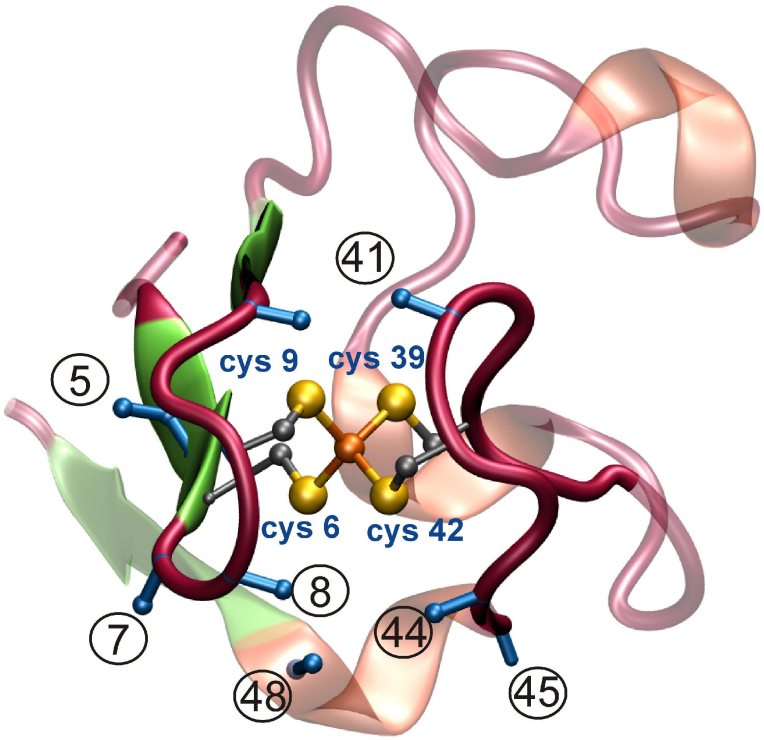

Figure 3.1: **Rubredoxin (Rd) crystal structure from *Cp* (PDB code 1IRO) with 53 amino acids and the iron-sulfur complex (ISC) in the center. The iron is covalently bond to four cysteine sulfur atoms belonging to two different protein loops (in red). $C_\alpha - C_\beta$ bonds (blue) with residue numbers depict amino acid side chains of the ISC that can have an impact on the Rd redox potential.**

3.2 Introduction

Iron-sulfur proteins (ISP) are ubiquitous in living systems [30–34]. Rubredoxin (Rd) is a redox-active protein and belongs to the simplest type of iron-sulfur proteins. Among its function is to store and transfer electrons to alkane hydroxylase from Rd reductase. The alkane hydroxylase belongs to a large class of membrane proteins of interest as biocatalyst for the production of alcohols, fatty acids and epoxides [35, 36]. The Rds under study possess from 52 to 54 amino acids except for one, which has 45 residues. The redox-active iron sulfur complex (ISC) in Rd consists of a single iron, ligated to four sulfur atoms of cysteine residues (see Fig. 3.1). The fact that the ISC in Rd contains only a single iron facilitates quantum chemical computations considerably, since anti-ferromagnetic coupling appearing in multi-nuclear ISCs is absent [7, 37–42]. Studies on ISPs and corresponding model systems have demonstrated that several factors are important to understand the properties of electron transfer active proteins [5–8, 31, 32, 34, 38, 41, 43–45]. These are number, types and strengths of H-bonds between ISC and specific amino acids [6, 8, 46–50], polarity and protonation states of the surrounding residues [51, 52], degree of solvent exposure of the ISC [5, 8, 45, 53] and quite generally the ISC electrostatic environment defined by the boundary between protein and solvent [45]. Using NMR spectroscopy, Lin et al [47, 48] found a correlation between redox potentials of mutant Rds from *Cp* and the H-bond strengths of the six amide H-bonds with ISC. They predicted variations of $NH \cdots S$ distances ranging from 2.2 Å to 2.8 Å and concluded that these are essentially responsible for the variations of redox potentials of different mutant Rds from *Cp*. However, the mutations of Rd do not only vary the H-bond strengths but also conformations, charge distributions and electrostatic boundary between protein and solvent that all can contribute to the shift in Rd redox potentials [8, 45]. Hence, one aim of the present study is to study theoretically the influences of these different factors on Rd redox potentials.

Besides these obvious factors also more subtle conformational details of the Rd-like ISC structure may influence its redox potential [54]. In this context it is worth mentioning that the ISC structures of Rds vary with the redox state [55] and differ from the crystal structures of corresponding small ISC Rd-like models [8, 56]. Such conformational changes of Rd-like ISC are quite important, as steric constraints imposed by the protein could alter the geometry and energetics of the ISC shifting its redox potential [8, 56]. This is why quantum chemical results obtained from small ISC model systems are often of limited value, making it necessary to consider larger ISC models [57]. These can model the protein environment more faithfully, yield higher accuracy, but introduce new problems, since these models may possess several energy minima of different geometry [58].

One of the challenging aspects of Rd function is to understand why its electron transfer behavior differs between Rds from mesophilic *Clostridium Pasterianum* (*Cp*) (prefers room temperature and denaturates at high temperatures) and thermophilic Pyrococcus furiosus (*Pf*) [59] (grows optimally at 90^o C) albeit structures and se-

quences are similar, see Table 3.1. The largest RMSD of backbone atoms is 0.62 Å, obtained between the crystal structures from *Cp* (PDB id 1IRO) and from *Pf* (PDB id 1CAD), while their sequence similarity [60] is about 70%. At the same temperature the difference in redox potentials reported by the same group was nearly 90 mV (Rd from *Cp* -55 mV; Rd from *Pf* $+31$ mV at $T = 25^oC$) [59]. These two very similar Rds were the subject of many experimental and theoretical studies during the past years [5, 51, 52, 55, 59, 61–72] to elucidate the reasons for the difference in the redox potentials. A number of these studies focused on amino acids in positions 8, 41, 44 and 45 (see Fig. 3.1 and Table 3.1) for which several mutant Rds from *Cp* have been crystallized [70, 71] and studied electrochemically [51, 52, 67] or by modeling [55]. Comparing the sequences of the Rds from *Cp* and *Pf*, (Table 3.1) one finds also other residues close to the ISC (for instance 5, 7, 48) that differ between the two species and may influence the Rd redox potentials as shown in this study. Other sequence variations occur on the protein surface and may be relevant for differences in thermo-stability between these two proteins. It has been suggested, that one of the factors enhancing the thermo-stability of proteins from thermophilic species are electrostatic interactions among oppositely charged groups (salt-bridges) [73–76]. However, in the Rd crystal structures no significant differences in the number of salt-bridges could be observed.

Protein cofactor redox potentials computed by evaluating electrostatic energies in continuum dielectric models [11, 15, 17–23, 26] yielded agreement with measurements for protein cofactors as different as hemes [11, 18, 19, 22], chlorophylls [23] and quinones [20–22] in different types of proteins. In these approaches measured redox potentials of appropriate model systems in solvents were used as reference values to compute the shift in redox potentials between solvent and protein environment by electrostatic energies. Since for Rd-like ISC such redox potential values were not available, we introduced in the present study ISC model compounds whose redox potentials were obtained by a combination of *ab initio* quantum chemical and electrostatic energy computations [8, 28]. Redox potentials in Rds were computed with a newly developed extended version of program Karlsberg$^+$ [24, 27], which

Table 3.1: **Sequence alignment of seven different species of Rubredoxin (Rd) (one with two strains Dv^1 and Dv^2) of known crystal structures:** *Clostridium Pasterianum* (*Cp*), *Pyrococcus furiosus* (*Pf*), *Desulfovibrio Gigas* (*Dg*), *Desulfovibrio desulfuricans* (*Dg*), *Desulfovibrio vulgaris* **Hildenborough strain** (Dv^1) , *Desulfovibrio vulgaris* **Miyasaki strain** (Dv^2) , *Pyrococcus Abyssi* (*Pa*) **and** *Pseudomonas Aeruginosa* (*Ps*).

Rd	1 . . . . 10. . . . . 20. . . . . 30. . . . . 40. . . . . 50. . . .
Cp	M K K Y T C T V C G Y I Y N P E D G D P D N G V N P G T D F K D I P D D W V C P L C G V G K D Q F E E V E E
Pf	A K W V C K I C G Y I Y D E D A G D P D N G I S P G T K F E E L P D D W V C P I C G A P K S E F E K L E D
Dg	M D I Y V C T V C G Y E Y D P A K G D P D S G I K P G T K F E D L P D D W A C P V C G A S K D A F E K Q
Dd	M Q K Y V C N V C G Y E Y D P A E H D N V P F D Q L P D D W C C P V C G V S K D Q F S P A
Dv^1	M K K Y V C T V C G Y E Y D P A E G D P D N G V K P G T A F E D V P A D W V C P I C G A P K S E F E P A
Dv^2	M K K Y V C T V C G Y E Y D P A E G D P D N G V K P G T S F D D L P A D W V C P V C G A P K S E F E A A
Pa	M A K W R C K I C G Y I Y D E D E G D P D N G I S P G T K F E D L P D D W V C P L C G A P K S E F E R I E
Ps	M R K W Q C V V C G F I Y D E A L G L P E E G I P A G T R W E D I P A D W V C P D C G V G K I D F E M I E

computes pK_a values and redox potentials in proteins by optimizing not only hydrogen atom positions, but also amino acid side chains and potential salt-bridge geometries. This approach was extended for the present study to compute redox potentials of the ISC in Rd.

In this study, we try to understand how Rd proteins from different species tune their ISC redox potential by varying amino acid composition and protein conformation. We quantify how much the dielectric environment affects the redox potentials of different Rd mutants from *Cp* by modeling the Rd structures using the polypeptide backbone from the WT structure combined with side chain rotamers taken from the crystal structure of the mutants while keeping the backbone amide H-bond geometries with the ISC invariant. We also investigated the role of salt-bridges to understand the redox potential differences between mesophilic and thermophilic Rd proteins. Furthermore, we consider the conformational variations observed in Rd crystal structures and evaluate the influence they have on Rd redox potentials.

3.3 Method

3.3.1 Electrostatic computations

All redox potentials reported in this work are based on electrostatic potentials obtained by numerical solution of the linearized Poisson-Boltzmann equation (PBE) using the program APBS [77, 78]. A short description of the linearized PBE is given in Appendix A. The protein was described as a set of atomic partial charges embedded in an inhomogeneous dielectric continuum where the dielectric constant was set to $\varepsilon_p = 4$ inside the protein and $\varepsilon_w = 80$ outside for bulk water. The boundary interface between protein and solvent lumen was calculated by the molecular surface routine implemented in APBS using a solvent probe radius of 1.4 Å. Ionic strength of potassium chloride was included implicitly at a concentration of 100 mM.

3.3.2 Rubredoxin model compound

Ab initio quantum chemical computations to obtain the redox potential of the Rd-like ISC model $[Fe(SCH_2CH_3)_4]^{-1,-2}$ were performed recently [8]. In water the redox potential of this model compound was computed to be $-15\ mV$ for a model compound with S_4 symmetry, while it was $+56\ mV$ for C_2 symmetry, the symmetry type prevalent in Rds [8, 56]. A larger ISC model that includes the six amide H-bonds as in Rd (but without including amino acids side chains), Fig. 1.3 yielded a redox potential of $+57\,mV$ with a dielectric constant of $\varepsilon_p = 20$ corresponding to protein environment [8]. Unfortunately, this large ISC model that includes the polypeptide backbone, is in conflict with the CHARMM force field, were the polypeptide backbone charges add up to zero. Combining an ISC model conflict free with the CHARMM force field to perform electrostatic energy computations in Rd we needed a small ISC model. Therefore, we considered the alchemical reference model $[Fe(SCH_2)_4]^{-1,-2}$ as described above. For this ISC model, a redox potential

in water of $+112\ mV$ was used for the electrostatic energy computations of the ISC in Rd. The atomic partial charges of the ISC model in Rd are presented in Table C.1

3.3.3 Redox potential computations in proteins with multi-conformers

For the electrostatic computations of the Rd redox potentials we employed a modified new version of Karlsberg$^+$ [24, 27] available in the web [79], which we used in the past primarily for accurate pK_a computations. Karlsberg$^+$ combines classical electrostatic energy computations with pH-dependent conformational relaxation of salt-bridges and H-bonds inside proteins. A brief description can be also found in Appendix A. In short, Karlsberg$^+$ tries to predict alternative atom positions for side chains of basic and acidic residues involved in salt-bridges under high and low pH conditions where these salt-bridges are generally not stable any more. It does so by generating pH adapted conformations (PACs) that are obtained by "self-consistent" geometry optimizations of the input crystal structure combined with random changes of side chains of basic and acidic residues. Here, we consider redox rather then pH dependence. Accordingly, we introduced redox adapted conformations (RACs) at ambient pH (pH 7) for a given Rd redox state in the same spirit as we introduced PACs before to describe the pH dependence of protonation patterns [24].

Self-consistent geometry optimization solves the problem to determine the most likely occupied protein conformations without knowing its most likely protonation pattern and vice versa. Therefore, Karlsberg$^+$ performs an iterative procedure analogous to quantum mechanical self-consistent energy computations. First, Karlsberg$^+$ calculates an initial protein protonation pattern at a high dielectric constant of $\varepsilon_p = 80$ everywhere (to avoid unphysical protonation pattern, which may easily appear initially) by adding and optimizing hydrogen atoms in the crystal structure with standard protonation (acids deprotonated and bases protonated). Based on this first guess of protonation pattern Karlsberg$^+$ performs geometry optimizations (at ambient pH and given redox state using the CHARMM22 [80, 81] force field with $\varepsilon_p = 1$ everywhere for all iteration steps) of amino acid side chains (including hydrogens) involved in salt-bridges and a selection of others that may influence the cofactor redox potential starting with a set of 30 structures with randomized side chain geometries for the considered amino acids. The resulting lowest energy global conformer of the protein is used in the next step to re-evaluate the protonation pattern by electrostatic energy computations (from now on with $\varepsilon_p = 4$ in the protein and $\varepsilon_w = 80$ outside). If it changes, the geometry optimization step is repeated using the new protonation pattern. The cycle is repeated until the protonation pattern remains constant at a given pH and redox state. With this procedure five RACs are generated for each redox state at ambient pH starting with a different random seed in each case. Finally, Karlsberg$^+$ computes redox titration curves of the protein using the ensemble of generated RACs with their electrostatic energies. This is done by application of a Metropolis-Monte-Carlo (MMC) procedure

that samples the lowest electrostatic energy of protonation, redox and conformational states of the protein and allows calculating the redox potentials as proper Boltzmann-weighted thermodynamic averages.

In case crystal structures of the same protein are available from different authors and/or solved in different oxidation states (see Fig. 3.2) all these structures were introduced in the RACs and used in the Boltzmann averaging.

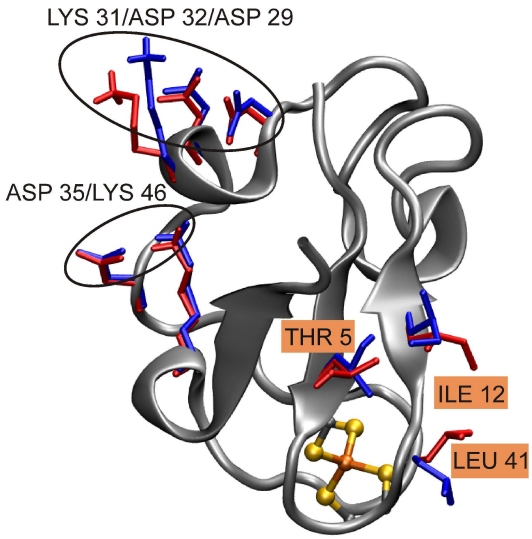

Figure 3.2: **Multiple side chain conformers of thr5, ile12 and leu41 observed in WT *Cp* in oxidized (blue, pdb id 1FHH) and reduced (red, pdb id 1FHM) state, that influence the computation of the Rd redox potentials. The OH group of thr5 is pointing towards the ISC in the oxidized state (i) while leu41 opens in the reduced state (ii). The conformation of ile12 changes as a side effect of these changes. We also highlight the two salt-bridges observed in *Cp*, D29-K31-D32 and D35-K46.**

Besides the treatment of salt-bridges Karlsberg$^+$ can now also generate RACs with geometry optimized side chains of mutated residues (and of other electrostatically relevant side chains of varying geometry), which is useful when no experimental coordinates are available for them. Since the side chains of the mutated residues possess different volumes and shapes than the side chains they are replacing, we included also the side chains of the neighbor residues (around 4 Å from the mutated residue) in the optimization procedure to generate RACs. If for the same protein, crystal structures from two different species are available, it is instructive to built RACs that use the whole polypeptide backbone and chain conformers of all conserved residues from one protein but have inserted side chain conformers of the other protein structure for the non-conserved residues. In case side chains were found in multiple conformations in the protein crystal structure (see Fig. 3.3), RACs were generated for each combination of side chain conformers and used in the Boltzmann averaging.

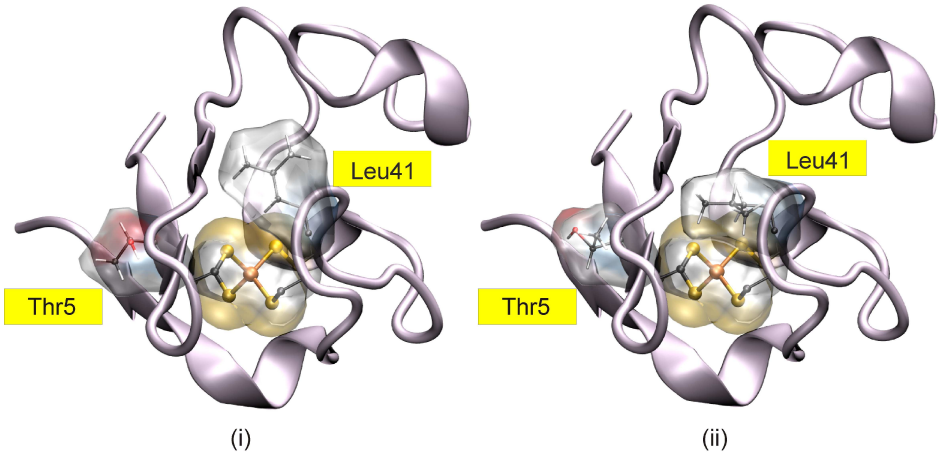

Figure 3.3: **Multiple side chain conformers of thr5 and leu41 observed in WT *Cp* (1IRO) that influence the computation of the Rd redox potentials. The OH group of thr5 is pointing towards the ISC in the oxidized state while leu41 opens in the reduced state. We indicate the changes in the dielectric environment in the neighborhood of the ISC produced by these changes in conformation**

Relaxing the conformations of amino acid side chains can also be quite useful, if a protein crystal structure has structural deficiencies. This is for instance the case for Rd crystal structures from *Cp* mutants that were solved as trimers [53, 71] and tetramers [9] where some side chains belonging to different monomers are in too close contact and needed to be relaxed.

In summary Karlsberg$^+$ [24, 27] consists of three modules: (i) for generating PACs or RACs, Karlsberg$^+$ employs the molecular mechanics software package CHARMM [80, 81], (ii) for computing electrostatic energies the Poisson-Boltzmann solver APBS [77, 78] is used and (iii) for performing statistical averages over protonation pattern and conformations (inherent in PACs or RACs) an MMC algorithm is used, which is a re-implementation of our legacy program Karlsberg [26].

3.3.4 *FeS*-proteins

The experimental information of atomic coordinates of all considered Rd in this study were taken from the protein database (PDB). These are the WT structures of Rds in the oxidized state from *Cp* [71, 82, 83], *Pf* [65, 84, 85], *Pyrococcus abyssi* (*Pa*) [9, 50], *Desulfovibrio vulgaris* (*Dv*) [86–88], *Desulfovibrio gigas* (*Dg*) [89, 90], *Desulfovibrio desulfuricans* (*Dd*) [91, 92], and *Pseudomonas Aeruginosa* (*Ps*) [36] (the latter was taken from the Rd-Rd reductase complex). We also considered Rd crystal structures in the reduced state, if available. These are from *Cp* (WT [55] and L41A mutant [70]) and from WT *Pf* [84]. The sequence alignment of Rds from the seven different species considered here is given in Table 3.1. More information regarding PDB codes, structure resolutions, redox states and literature are given in Table D.1 in the appendix. We also used crystal structures of mutant Rds from *Cp*

(L41A [70], V44L, V44A, V44G and V44G/G45P [71]) and from *Pa* (W4L/R5S and W4L/R5S/A44S [9, 50]). However, we excluded structures from NMR experiments. All Rd crystal structures were pair-wise superimposed relative to the WT structure from *Cp* (PDB code 1FHH) using the Kabsch algorithm [93] considering the atoms of ISC only (iron, and sulfurs and $C\beta$ atoms of the four ligating cysteines) to detect amino acids whose side chains are in different conformations (see Table D.2).

Hydrogen atoms were added to the available crystal structures of Rd using Karlsberg$^+$ as explained in section 3.3.3. If not stated otherwise, we computed the Rd redox potentials from an ensemble of RACs generated by Karlsberg$^+$ varying the geometries of salt-bridges and of side chains of mutated residues if no crystal structures are available. Some Rd crystal structures contain several proteins per unit cell (see Table D.1). In those cases we generated RACs for each of the slightly different monomer structures to compute the Rd redox potentials. The same procedure was used in cases where several Rd crystal structures of the same species were available from different authors (see Table D.1 in the Appendix). The crystal structure of WT Rd from *Cp* (5RXN [82]) was excluded, since it involved a sequence mismatch with the other three Rd structures from *Cp* (1IRO, 1FHH, 1FHM).

ISC redox potential contributions due to specific amino acids were analyzed by setting the charges of specific side chain atoms to zero while computing the Rd redox potential. The corresponding shift of Rd redox potential was obtained as Boltzmann average over all RACs.

3.3.5 Measured Rubredoxin redox potentials

Measured redox potentials for Rds WT and mutants from *Cp* are listed in Table D.1. Redox potentials of WT and mutant Rds from *Cp* measured by different groups vary by about 20 mV. These variations may be due to different measurement methods and the usage of redox modifiers (like poly-lysine) that allow the observation of stable square voltammetry in particular for negatively charged proteins like Rd [67, 73]. Unfortunately, the resulting measured redox potentials [67] may depend on the usage of such modifiers. They can slightly up-shift redox potentials rendering an interpretation of redox potential shifts from different labs more difficult. Furthermore, there are small variations of pH and temperature where Rd redox potentials were measured (see *Pf*, for example) (Table D.3). Accordingly, Rd redox potentials are more positive at lower than at higher pH [94] and decrease with higher temperatures [59]. In our redox potential computations we assume standard conditions, i.e. pH 7 and 25^{o}C and no adjustment of measured redox potential due to the use of redox modifiers was considered.

In this study we considered five different aspects to characterize how the Rd redox potentials depend on different factors:

1. Rd redox potentials of different species and their mutants were computed using all data from accessible crystal structures (multiple side chain conformers and

structures of different monomers in the unit cell) but otherwise optimizing hydrogen atom positions only to study the dependence on crystal structure data.

2. We considered the same Rds but performed now extensive geometry optimizations to study the influence on Rd redox potentials due to variation side chain conformations of specific amino acids close to the ISC or involved in salt-bridges.

3. To study the dependence of the Rd redox potentials on H-bond geometry, side chain conformers and charges as well as electrostatic boundary we focused on mutant Rds from a single species (*Cp*), where sequence and structure variations are much smaller than between different species. Here, the generated RACs for different mutant Rds from *Cp* were based exclusively on a single Rd crystal structure from WT *Cp* (PDB id 1IRO). Thus, the polypeptide backbone remain unchanged.

4. We consider the Rds from mesophilic *Cp* and thermophilic *Pf* to discuss different factors that influence the Rd redox potential.

5. The protein backbone variation close to the ISC observed in Rd crystal structures from *Pa* (mutant W4L/R5S) allows studying computationally how geometry variations of amide H-bonds with ISC sulfurs influence the Rd redox potential.

3.4 Results and Discussion

3.4.1 Rubredoxin redox potentials in crystal structures

Based on the Rd crystal structures, listed in Table D.2, we generated RACs corresponding to the oxidized and reduced state of ISC by self-consistently optimizing only the hydrogen atom coordinates using Karlsberg$^+$ as explained in the methods section. In case there was more than one monomer or multiple side chain conformers available, we created a RAC for each possible combination in the same manner. There are crystal structures corresponding to both oxidation states of ISC for WT *Pf* as well as WT and L41A mutant Rd from *Cp*, so we derived the RACs from both crystallographic states in this case. Otherwise, we generated RACs corresponding to the reduced state of the ISC from the corresponding crystal structure in the oxidized state. In four Rd crystal structures (WT and V44A, V44G, V44L mutant Rds from *Cp*) atomic coordinates of the C-terminal residue (E54) are missing (E53$C_\alpha - Fe$ distance 18 Å). The missing atoms were modeled yielding computed redox potentials that deviated by less than 4 mV from the corresponding values in absence of E54. Henceforth all computed redox potentials of these four Rds refer to the crystal structures without the modeled C-terminal residue.

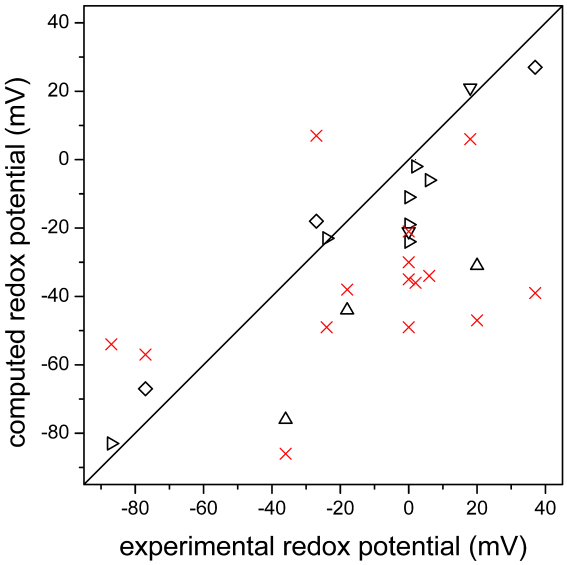

Figure 3.4: **Comparison of measured and computed redox potentials of Rds with fifteen different sequences using the corresponding crystal structures. These are WT Rds from eight different species/strains (*Cp*, *Pf*, *Pa*, *Dg*, *Dv* (H), *Dv* (M), *Dd*, *Ps*) and seven mutant Rds from *Cp* (V44A, V44L, V44A/G45P, V44G, L41A) and from *Pa* (W4L/R5S, W4L/R5S/A44S). The symbols × refer to computations based on crystal structures where only hydrogen atoms were optimized (RMSD 42 mV). The open symbols ($\diamond, \triangle, \triangledown, \triangleright$) refer to computations where in addition, side chains of residues close to the ISC or involved in salt-bridges were optimized using a larger number of RACs (from 16 to 176) (RMSD 16 mV). For the twelve Rds marked by triangles ($\triangle, \triangledown, \triangleright$) crystal structures are only available for the oxidized states. For the three Rds marked by $\diamond$ crystal structures are also available for the reduced states. The three Rd redox potentials from *Pa* denoted by ($\triangle$) were measured in the same lab [9] using poly-lysine as redox modifier that can up-shift Rd redox potentials (see discussion in text). Rd redox potential values from two species (*Cp* V44A/G45P, WT *Ps*) denoted by ($\triangledown$) were not measured but estimated. Redox potentials are listed in Table 3.2.**

In these preliminary computations the correlation between measured and computed Rd redox potentials is low (RMSD of 42 mV; see in Fig. 3.4; corresponding values are listed in Table 3.2. Results of similar quality were reported before [5] using solely Rd crystal structures optimizing only hydrogen atom positions as it was done for the preliminary computations in the present study. Some improvement was obtained when the computed Rd redox potentials were based on structures from molecular dynamics (MD) simulations [5, 72]. These MD based approaches generally involve global changes in Rd structures making it difficult to quantify the different redox potential contributions of a specific Rd protein or mutant. In the present study, only moderate structural modifications of the Rd crystal structures where considered making it easier to identify specific influences of structural features on redox potentials of WT and mutant Rds from different species. The results of our computations of Rd redox potentials involving such small conformational changes are presented in the next two sections.

Table 3.2: List of calculated Rd redox potentials using crystal structure information and comparison with measured values E^o_{exp}. We present the results using two levels of approximation: optimization of hydrogen positions E^o_{comp1} and optimization of side-chain and salt-bridges conformations E^o_{comp2}. The corresponding data is plotted in Fig. 3.4.

rubredoxins variants		redox potential mV		
		E^o_{exp} [a]	E^o_{comp1}	E^o_{comp2}
Clostridium pasterianum (*Cp*)	WT	-77	-57	-67
	L41A	-27	7	-18
	V44A	-24	-36	-2
	V44G	0	-36	-2
	V44L	-87	-54	-83
	V44A/G45P	18	6	21
Desulfovibrio gigas (*Dg*)	WT	6	-34	-6
Desulfovibrio vulgaris (*Dv* H)[c]	WT	0	-35	-21
Desulfovibrio vulgaris (*Dv* M)[d]	WT	-5	-21	-19
Desulfovibrio desulfuricans (*Dd*)	WT	0	-49	-11
Pyrococcus furiosus (*Pf*)	WT	37	-39	27
Pyrococcus abyssi (*Pa*)	WT	-18	-38	-44
	W4L/R5S	-36	-86	-76
	W4L/R5S/A44S	20	-47	-31
Pseudomonas aeruginosa (*Ps*)	WT	0	-30	-24

[a] The complete list of measured redox potential an references is presented in Table D.3,
[b] Hildenborough strain,
[c] Miyasaki strain.

3.4.2 Rubredoxin redox potentials with redox adapted conformations

Considering the same crystal structures as used in the preliminary computations (preceding section) we calculated the Rd redox potentials again using a larger number of RACs with optimized side chains of a selected set of residues close to the ISC (5, 7, 8, 41, 44, see Fig. 3.1) and the ones involved in salt-bridges. By mutational analysis of the Rd from *Cp* (discussed in the next section) the aforementioned residues were identified to have strong influences on the ISC redox potential. The correlation diagram of measured and calculated Rd redox potentials of all fifteen Rds yields an RMSD of 15 mV (open symbols in Fig. 3.4; values listed in Table 3.2. This is a significant improvement compared to the results obtained by optimizing hydrogen atom positions only ($\times$ symbol in Fig. 3.4). For thirteen of these Rds redox potentials were measured, while in two cases (WT Rd from *Ps* and mutant Rd V44A/G45P from *Cp*) only estimates were available. For the two Rds with estimated redox potentials ($\bigtriangledown$ in Fig. 3.4), which we included in the RMSD value, we did not observe a lower quality of agreement. The RMSD increases slightly

(17 mV), if we consider the twelve Rds where crystal structures are available only for the oxidized states (▷ in Fig. 3.4), but becomes smaller (8 mV), for the three Rds (◇ in Fig. 3.4) where crystal structures are available for both redox states that were used to generate the RACs. The largest discrepancies are systematic deviations that occur for redox potentials of the three Rds from *Pa* △. They were measured in the same lab [9, 50] using poly-lysine as redox modifier, which may cause an up-shift of the measured redox potential by about 20 mV [73].

The relatively large differences in the sequences of the considered Rds from seven different species make it difficult to explain how specific amino acids contribute to the shifts of redox potentials. However, there is a trend: replacing small by large hydrophobic amino acids in positions 8, 41 and 44 decreases the solvent accessibility of ISC and consequently lowers the redox potential [67]. Amino acids like leucine are not only voluminous but due to their long flexible side chains they can also possess several local minima which makes it more difficult to explore their influence on Rd redox potentials.

3.4.3 Redox potentials in Rubredoxin *Cp* mutants

To assess the structure-function relationship between the mutant residues and the ISC redox potential we reconstructed the structures of all mutant Rds from *Cp* for which the ISC redox potential has been measured (amounting to a total number of 15, see Table 3.3) using the backbone structure of the oxidized WT Rd taken from *Cp* (PDB id: 1IRO) as a scaffold and reproduce the corresponding mutant Rd redox potentials. Mutations are considered at the sequence positions 8, 41, 44 and 45. With Karlsberg$^+$ we generated RACs with varying side chain conformers in six sequence positions (5, 8, 41, 44, 45 and 48, see Fig. 3.1) including the mutated residue and its direct neighbors. The conformational ensemble also included RACs with varying coordinates of residues involved in salt-bridge networks (D29-K31-D32, D35-K46, E51-K2-E53). Since the protein backbone atom coordinates were kept invariant in all of these modeled Rd structures, the H-bond geometries of the ISC involving only backbone amide groups did not vary with the mutant Rds and its redox states. Hence, we can study how the side chain and corresponding dielectric boundary variations are influencing the Rd redox potentials independent of possible variations of backbone H-bond geometries with the ISC. With these RACs involving optimized amino acid side chain geometries the comparison of computed and measured Rd redox potentials yielded a surprisingly low RMSD of only 14 mV (Fig. 3.5; values listed in Table 3.3). Again this is a considerable improvement compared to the preceding results where only the hydrogen atoms were optimized (× symbols in Fig. 3.4).

No systematic deviation between measured and computed Rd redox potentials could be detected although variations in the geometry of the amide H-bonds involving the ISC were not considered. Hence, at least for these Rds, the variation of the redox potentials between the different mutants can be very well explained by other factors

Table 3.3: **Sixteen measured and calculated redox potentials of Rds from *Clostridium pasterianum* (*Cp*), (WT and 15 mutants) where the structures were modeled using WT Rd from *Cp* (1IRO). Computed results use two levels of approximation: (1) generating two self-consistent conformers with optimized hydrogen atom positions corresponding to the oxidized and reduced redox state, respectively, $E^o_{H\ only}$, and (2) as before but including additional RACs for residue side chains in positions (5, 8, 41 and 44) and residues involved in salt-bridges, $E^o_{H\&R}$. The corresponding data are plotted in Fig. 3.5.**

Clostridium pasterianum WT/ mutants	redox potential mV E^o_{exp}[b]	$E^o_{H\ only}$	$E^o_{H\&R}$
WT[b]	-77	-51	-60
L41A[b]	-27	-43	-40
V8A	-44	-13	-38
V8D	-28	-64	-34
V8G	-7	+42	+6
V8I	-81	-43	-66
V8L	-82	-51	-68
V8R	-15	-13	0
V44A[b]	-24	-27	-44
V44G[b]	0	-29	+10
V44I	-53	-48	-55
V44L[b]	-87	-59	-70
V8G/V44G	+39	+31	+24
V8I/V44G	-13	-31	-35
V8I/V44I	-55	-40	-62
V44A/G45P	+18	+21	+14

[a] The complete list of measured redox potential and references is presented in Table D.3,
[b] These Rd *Cp* mutants have an available crystal structure. Their redox potential using crystallographic information is presented in Table 3.4.1.

than the amide H-bond geometry around the ISC. One such important factor seems to be the ISC solvent accessibility. In the high resolution Rd crystal structure from WT *Cp* (1IRO) several residues (T5, P15, K31, L41, E50) possess multiple side chain conformers. Interestingly, the side chain conformers of T5, K31 and L41 (and also of I12) vary in the crystal structures of reduced and oxidized Rds (see Fig. 3.2). The most populated RACs of the oxidized and reduced states contain the multiple conformers of L41 (Fig. 3.6). We observed that L41 is less buried in the reduced state and thus opens a small cavity near to the ISC. This open L41 conformer correlates with results of MD simulations, were a water molecule near L41 gets closer to the ISC in the reduced state [55, 70]. We forced the L41 side chain not to switch to the

open conformer in the reduced state, which down-shifted the computed Rd redox potential by 34 mV. Alternative side chain rotamers for T5, T7, V8, I12, and Q48 were modeled showing only a small variation of redox potential (about 10 mV), since these alternative conformations were only marginally populated in the RACs possesing a large weight. Other multiple side chain conformers involving P15, K31 and E50 found in the Rd crystal structure from WT *Cp* (1IRO) had also practically no influence on the Rd redox potential.

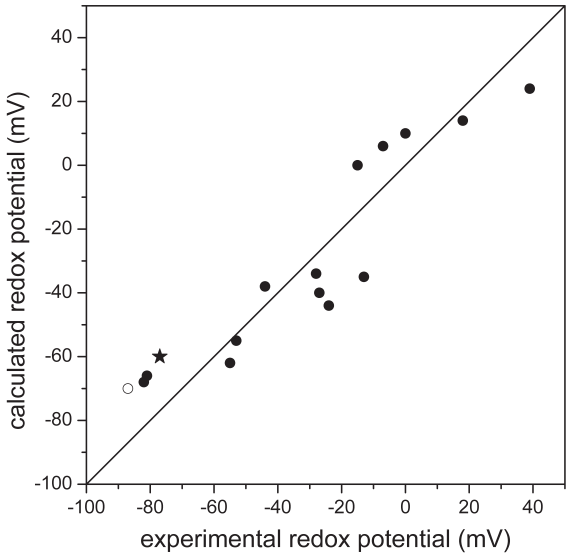

Figure 3.5: **Comparison of fifteen experimental and computed redox potentials of Rds from *Cp*. Based on the WT Rd crystal structure from *Cp* (1IRO) the structures of fourteen single and double mutants (V8A, V8D, V8G, V8I, V8L, V8R, V44A, V44G, V44I, V44L, V8G/V44G, V8I/V44G, V8I/V44I, V44A/G45P, L41A) were modeled and the redox potentials were computed (close circles, mutant Rds; star WT Rd). For modeled Rd mutant V44L, where a crystal structure is available, the mutated side chain was generated with the same rotamer conformation as the crystal structure (open symbol, Rd mutant V44L). For V44A, V44G, V44A/G45P, which also have a crystal structure, this procedure was not necessary, as they have shorter side chains.**

The five salt-bridges (K2-E51, K2-E52, K31-D29, K31-D32, K46-D35) present in the WT *Cp* crystal structure (1IRO) are present in all RACs of mutant Rds from *Cp*. Additional charged residues introduced in the mutants V8D and V8R do not lead to the formation of additional salt-bridges. In both mutants the redox potentials are up-shifted compared to WT Rd (measured: 49 mV and 62 mV, computed: 26 mV and 58 mV, respectively). The up-shift is surprising for the mutant V8D, since a negative charge (D8 was found to be deprotonated) is introduced that is expected to stabilize the oxidized state of ISC and, therefore, decrease its redox potential. Our computations can qualitatively explain this effect: Asp8 is solvent exposed and does not interact directly with the ISC that becomes more solvent exposed in this mutant, thus, up-shifting the redox potential.

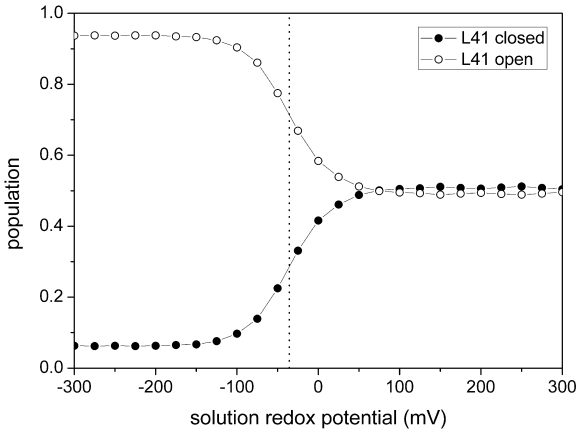

Figure 3.6: **The ISC redox potential is computed as Boltzmann average of all redox adapted conformations (RACs). To illustrate the contribution from different RACs to the ISC redox potential, we considered only two RACs generated with the two possible local conformers (L41 open and L41 closed) adopted by L41 in the crystal structures of the WT Rd from *Cp* in the oxidized state (PDB id 1IRO). Using the combination of these two local side chain conformers we obtained one RAC for the oxidized state (close symbols) and one RAC for the reduced state (open symbols). The two RACs with local conformer L41 close/open are both populated in the oxidized state (as in the crystal structure) while the conformer with L41 open is clearly more populated in the reduced state. The dash line indicates the midpoint potential E^o of these two RACs. In the computation of the ISC redox potential of Rds (open symbols in Fig. 3.4 we used a larger number of RACs involving different conformers of the amino acids 5, 7, 8, 12, 44 and 48.**

3.4.4 Differences between Rubredoxins from *Cp* and *Pf*

Understanding redox potential variations between the Rds from the thermophilic (*Pf*) and mesophilic (*Cp*) species have been the concern of many studies [5, 52, 53, 55, 59, 62, 63, 65, 72, 84, 95]. It has been suggested, that the presence of A44 in Rd from *Pf* contributes significantly to an up-shift of the Rd redox potential [53]. However, there are variations in the Rd sequences from *Cp* and *Pf* at 24 positions that may influence the redox potentials. We computed the contributions to the ISC redox potential per amide H-bond by setting to zero the corresponding backbone charges of the NH group and its direct neighbor groups ($C=O$, $C_\alpha H$). A detailed list of these contributions is given in Table 3.4. Accordingly, we observed a positive shift of the Rd redox potential due to the amide H-bonds, which is on average 63 mV per H-bond in agreement with *ab initio* quantum chemical computations on ISC model complexes [8]. However, as these six amide H-bonds are inherent to all considered Rd structures, only differences in H-bond strengths can contribute to the differences observed for Rd redox potentials. In case of Rd from *Cp* and *Pf*, the difference of total contribution of amide H-bonds is only 21 mV (Table 3.4).

There are 3 (5) positively and 13 (13) negatively charged residues in the Rd from *Cp* (*Pf*) without considering terminal groups and the ISC. By setting to zero the atomic partial charges of the corresponding side chains we observed downshifts of the Rd

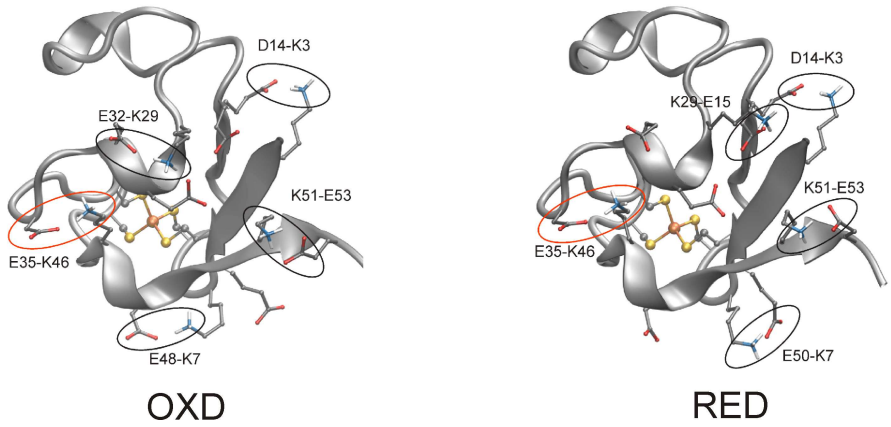

Figure 3.7: **Some relevant side chain conformers of the thermophilic Rd** *Pf* **showing the salt-bridges formed on the protein surface for the oxidized (left) and reduced state (right), although all salt-bridge patterns are observed in both states. Due to differences in sequence, these salt-bridges are not observed in the mesophilic Rd from** *Cp*. **The presence of Lys (Arg) in positions 6, 29 and 51 (Table 3.2) are characteristics of the thermophilic proteins** *Pf* **and** *Pa*. **The salt-bridge E50-K7-E48 is close to the ISC. Salt-bridges are observed in both oxidation states.**

redox potentials by $-63\ mV$ and $-38\ mV$ for *Cp* and *Pf*, respectively. Because the shifts in both species are qualitatively the same, the different composition in charged amino acids cannot explain difference in Rd redox potentials. The RACs generated for the two thermophilic Rds from *Pf* and *Pa* notably involve more salt-bridges than the corresponding crystal structures (see Fig. 3.7 and Fig. D.1). On the other hand, we found that the salt-bridges in Rd have in general only a small influence on the redox potentials (Table D.4), such that they cannot be used to explain the redox potential differences of the Rds from *Cp* and *Pf*. The contribution of the backbone is around 45 mV more positive for *Pf* than for *Cp*, from which less than the half (20 mV) is due to differences in H-bond strengths.

3.4.5 H-bonds with the ISC in *Pa*

The crystal structure of the (W4L/R5S) Rd mutant from *Pa* (1YK5) was solved at high resolution ($\sim$ 0.7 Å) in the oxidized state. It exhibits multiple side chain conformers for six residues (five residues have two and one three conformers) who are not too distant to influence the ISC. In addition the Rd crystal structure shows for cys9 two backbone conformations, one corresponding to the WT crystal structure the second with the amide plane between cys9-ile8 rotated by about 20^o and the amide plane between ile8-lys7 translated by about 0.13 Å. We considered this protein backbone variation to understand how the amide H-bond with the ISC sulfur can affect the Rd redox potential. Accordingly, the amide H-bonds formed by residues lys7 and ile8 possess in WT (mutant) Rd from *Pa* the lengths ($N-S$) of 3.5 and 3.6 Å (3.4 and 3.8 Å), respectively. Hence, in the mutant Rd from *Pa* one amide H-bond is shorter the other longer compared to the WT Rd from Pa.

Table 3.4: **Contributions to Rd redox potentials from two species, *Pf* and *Cp*. The different contributions are obtained as the difference of the full redox potential, E_{full} with the redox potential computed when the atomic partial charges of the corresponding molecular group are set to zero, E_{zero}.**

Pyrococcus furiosus (*Pf*) $E^o(full) = +26\ mV$ [a]		*Clostridium pasterianum* (*Cp*) $E^o(full) = -65\ mV$[a]	
NH-bond residue [b]	$[E^o_{full} - E^o_{zero}]$	NH-bond residue[b]	$[E^o_{full} - E^o_{zero}]$
Ile 8	58	Val 8	51
cys 9	81	cys 9	73
tyr 11	55	tyr 11	59
ile 41	79	leu 41	74
cys 42	59	cys 42	56
ala 44	58	val 44	56
average amide NH-bond	65	average amide NH-bond	62
all charged residues[a]	-38	all charged residues[a]	-63
backbone	515	backbone	471

[a] $E^o(ref)$ was obtained using the most populated RACs of *Cp* and *Pf*, six RACs in the case of *Pf* and five in the case of *Cp*, the small amount of RACs yields a slight variation of ISC redox potential used as a reference from the reported values in main text.

[b] The amide H-bond is defined by the NH group of the residue listed and the two neighbor atoms ($C = O$, $C_\alpha H$),

[c] The contribution due to charged residues in Rd Include the N-terminal group and if existing in the crystal structure also the C-terminal group.

For a careful case study on the influence of the amide H-bonds on the redox potentials, we modeled three different backbone conformations using the same side chain conformations of WT *Pa*, (1) varying amide H-bond with lys7, (2) varying amide H-bond with ile8, (3) varying both amide H-bonds and lastly, (4) varying both amide H-bonds and the side conformations of lys7 and ile8. Shortening of the amide H-bond with lys7 (case 1) yielded a redox potential up-shift of 18 mV while stretching the H-bond (case 2) yielded a down-shift by 21 mV. These shifts nearly cancel varying both amide H-bonds (case 3) yielding a small down-shift of 7 mV. Interestingly, when also the side chain conformations were varied (case 4), a redox potential up-shift of 23 mV was obtained. Extrapolating these results and averaging (case 1 and case 2), we can estimate that shortening an amide H-bond by 0.1 Å results in an up-shift of about 13 mV. For this estimate we considered no H-bond variation with the redox state. Nevertheless, this result demonstrates that the dependence of the Rd redox potentials on amide H-bond strengths can involve also a significant contribution from the variation of the side chain conformer.

To investigate the influence of an $S \cdots HO$ H-bond on Rd redox potentials, Bonisch et al. [50] generated the Rd triple mutant W4L/R5S/A44S from *Pa* whose Ser44 $OH-$group forms an additional H-bond with the ISC. In contrast to the corresponding double mutant W4L/R5S the triple mutant does not involve multiple backbone conformers at cys9. Hence, the six amide H-bonds with ISC remain intact. For the ISC H-bond involving an $OH-$group, computations on Rd-like ISC models showed an $O-S$ distance variation between 3.2 and 3.6 Å with a redox potential up-shift of about 90 mV [8]. The measured up-shift for the Rd triple mutant with respect to the Rd double mutant was 56 ± 20 mV [50], which is comparable to our computed value of 39 mV obtained using the crystal structure from the Rd triple mutant W4L/R5S/A44S from *Pa* (see Table 3.2). Interestingly, the ser44 side chain seems to be under strain in this Rd structure, since in our RACs we observed that ser44 can form either and H-bond with cys6 or cys42, with $O-S$ distances of 3.2-3.8 Å and 3.2-4.4 Å, respectively, where the H-bond with cys6 is more populated in the RACs.

Alternatively, using the crystal structure of the Rd double mutant W4L/R5S from *Pa*, we modeled the Rd triple mutant W4L/R5S/A44S from *Pa* that includes an extra $O-H \cdots S$ H-bond. In this model structure we optimized only the ser44 side chain allowing us to compute the influence of one H-bond without adding additional conformational changes. For this triple mutant, the up-shift in redox potential was 58 mV, that is in good agreement with previously computed values on ISC models [8] and in agreement with the estimate made by Bonisch *et al* [50] for this type of H-bond.

3.5 Conclusions

Continuum electrostatic energy computations were used on a set of Rd protein structures, which are the result of geometry optimizations that were performed self-consistently on crystal structures with the proper protonation pattern at given pH and solvent redox potential to evaluate cofactor redox potentials. Redox adapted conformations (RACs) were generated using a set of available crystal structures taking into account all combinations of available multiple side chain conformers and of optimized side chain conformers of mutated residues and residues involved in salt-bridges or close to the ISC. If only hydrogen atom positions were included in self-consistent optimizations of RACs, the RMSD between measured and computed redox potentials of Rds with fifteen different sequences was 42 mV, while the measured redox potentials vary only between -86 mV and $+31$ mV. This agreement result is enormously improved, if additional RACs corresponding to optimized salt-bridges and other important side chains were added to the electrostatic energy computations yielding an RMSD of 16 mV. For fifteen Rds (WT and fourteen mutants) from *Cp* where measured redox potentials are available, RACs were generated solely based on the WT crystal structure not varying the backbone. The computed redox potentials showed an RMSD with measured data of only 14 mV, while the measured redox potentials vary between -86 mV and $+39\,mV$. For these structures no vari-

ation of the amide H-bonds with the ISC was considered. This excellent agreement between measured and computed redox potentials does not support the general assumption that mainly the amide H-bond strengths are responsible for variations in Rd redox potentials. However, eliminating such an H-bond completely down-shifts Rd redox potential by about 63 mV. We estimated that a variation of the amide H-bond length by 0.1 Å can shift the Rd redox potential by 13 mV. Although the composition of charged groups and formation of salt-bridges differ considerably between the mesophilic Rd from *Cp* and the thermophilic Rd from *Pf* and are considered to be responsible for the difference in thermo-stability, their contributions to the redox potential difference between the two Rds was found to be insignificant. In summary, the variations in redox potentials of different Rds result from combinations of backbone and side chain variations, which lead to subtle changes of charge distribution and electrostatic boundary, while the amide H-bonds with the ISC play only a minor role.

Chapter 4

Understanding properties of cofactors in proteins: redox potentials of synthetic cytochrome b

Ana P. Gamiz-Hernandez, Gernot Kieseritzky, Artur. S. Galstyan and E. Walter Knapp

ChemPhysChem **2010**, 11, 1196-1206.
http://www3.interscience.wiley.com/journal/123362544/abstract

Contents

4.1 Contributions

- Computation of atomic partial charges for a heme model with two orientations of ligand histidines.
- Modeling from scratch of the atomic coordinates of an artificial cytocrome b (aCb) with heme ligated to two histidines.
- Modeling of 30 synthetic mutants from the initial aCb coordinates with two different heme conformations.
- Molecular dynamics simulation of the coordinates of the aCb with two different conformations.
- Computation of the redox potentials of all 31 hemes with two different heme conformations in the aCb.
- Investigation and discussion of factors contributing to differences in redox potential in aCb mutants.

4.2 Summary and discussion

Haehnel et al. [12] synthesized 399 different artificial cytochrome b (aCb) models. They consist of a template-assisted four-helix bundle with one embedded heme group. Their redox potentials were measured and cover the range from -148 to -89 mV. No crystal structures of these aCb are available. Therefore, we use the chemical composition and general structural principles to generate atomic coordinates of 31 of these aCb mutants, which are chosen to cover the whole interval of aCb redox potentials. We start by modeling the coordinates of one aCb from scratch. Its structure remains stable after energy minimization and during molecular dynamics simulation over 2 ns. Based on this structure, coordinates of the other 30 aCb mutants are modeled. The calculated redox potentials for these 31 aCb agree within 10 mV with the experimental values in terms of root mean square deviation. Analysis of the dependence of heme redox potentials on protein environment shows that the shifts in redox potentials relative to the model systems in water are due to the low-dielectric medium of the protein and the protonation states of the heme propionic acid groups, which are influenced by the surrounding amino acids. Alternatively, we performed a blind prediction of the same redox potentials using an empirical approach based on a linear scoring function and reach a similar accuracy. Both methods are useful to understand and predict heme redox potentials. Based on the modeled structure we can understand the detailed structural differences between aCb mutants that give rise to shifts in heme redox potential. On the other hand, one can explore the correlation between sequence variations and aCb redox potentials more directly and on much larger scale using the empirical prediction scheme, which - thanks to its simplicity - is much faster [11].

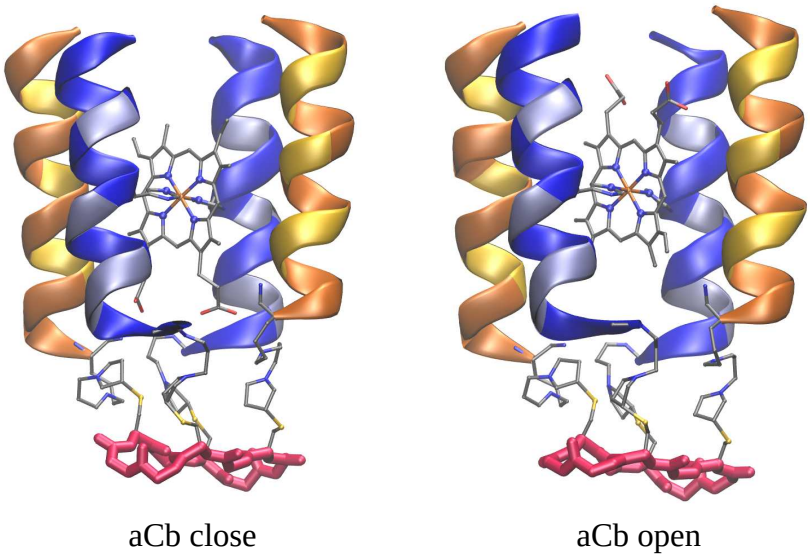

Figure 4.1: Two possible heme conformations in the artificial Cytochrome b (aCb) with propionic groups pointing inside the four-helix bundle (aCb close) or pointing towards the solvent (aCb open).

Appendix A

The model of a protein in solution and continuum electrostatics

Electrostatic effects play major roles in proteins [13, 14, 16] and the ability to quantify electrostatic interactions is essential for any structure-function correlation in biomolecules. These effects can be considered by a wide range of approaches, spanning from continuum dielectrics to atomistic representations and quantum mechanical calculations [14]. Each approach has its own scope and limitations and in general can be divided in three groups: all-atom, dipolar and continuum model. In the atomistic model, the molecular system is described as a collection of point charges that interact via a classical force field while in the dipolar model, this treatment is simplified by using a representation of the molecule or groups as dipoles. In the continuum treatment (also known as the Poisson-Boltzmann model), the protein and the solvent are described as a heterogeneous dielectric media.

The most detailed electrostatic computations correspond to a macroscopic solvent model that tries to describe the electrostatic interactions of the solvent with a dissolved protein whereas the protein is still represented in atomic detail. This approach has been employed in the Knapp group [15, 17–24] and it has been used in this work, where the protein is represented as a continuum with a low dielectric constant $\varepsilon_p = 4$ and individual atomic partial charges, while the solvent (water) is described as a continuum with high dielectric constant $\varepsilon_w = 80$ and without individual charges.

Figure A.1 shows a model for a protein in ionic solution consisting in three regions: the protein with immobile point charges, the solvent with mobile ions and a layer separating the protein from the solvent, called ion-exclusion layer which is penetrated by the solvent but remains inaccessible for the mobile ions. In the electrostatic continuum approach, the solvent (water) is not represented by explicit solvent molecules, but implicitly by a medium with high dielectric constant $\varepsilon_w = 80$. The interior of the protein, separated from the solvent by the solvent accessible surface, is assigned a low dielectric constant. At a first glance, one should expect this constant to be unity (as in vacuum) since the atoms of the molecule are all represented explicitly in this model. However, electronic and nuclear polarization effects not considered explicitly by the model require a larger dielectric constant to be more appropriate (for protein $\varepsilon = 4$ is generally used [96]).

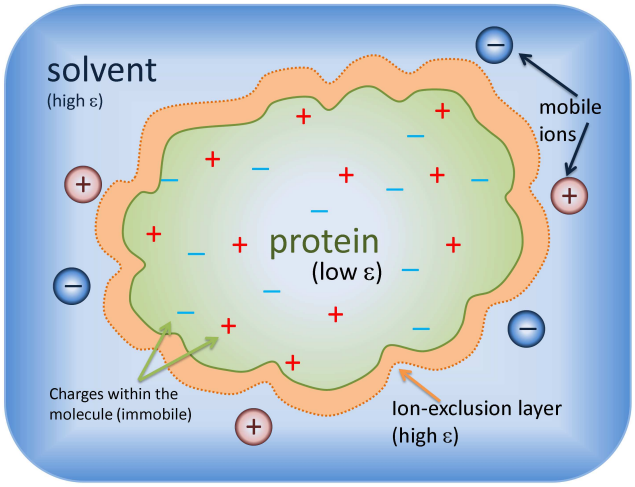

Figure A.1: **Schematic representation of the extended Debye-Hückel model for a solvated protein consisting of three regions: protein, ion-exclusion layer and solvent.**

Continuum electrostatic

According to classical electrostatics, a systems consisting only of charges in vacuum is described by the Poisson's equation,

$$\nabla \cdot \nabla\phi(r) = -\frac{\rho(r)}{\varepsilon_o} \tag{A.1}$$

$$\vec{E}(r) = -\nabla\phi(r), \tag{A.2}$$

where $\phi(r)$, $\vec{E}(r)$ and $\rho(r)$ are electrostatic potential, electric field and charge density as a function of the position r while ε_o is the vacuum permittivity (electric constant). For a condensed medium in which dielectric effects can be represented by a spatially dependent dielectric constant, $\varepsilon(r)$, equation A.1 becomes

$$\nabla \cdot [\varepsilon(r)\nabla\phi(r)] = -4\pi\rho(r), \tag{A.3}$$

if ions are present in the solution we need to apply the Debye-Hückel theory. Accordingly, considering a number of ions, n_i^o of type i per unit volume, if ze_i is the ionic charge, then electro neutrality demands that

$$\sum z_i n_i^o = 0. \tag{A.4}$$

The Debye-Hückel theory is based on the following two assumptions:

- Around any ion of type j, the charge distribution is assumed to be spherically symmetric.
- The charge density $\rho(r)$ follows a Boltzmann distribution law.

The first assumption corresponds to the approximation of each spherical ion by a point charge at the center and in particular for $\rho(r)$, the charge density of the ion, obeys

$$\int_a^\infty 4\pi r^2 \rho(r) dr = -z_j e, \tag{A.5}$$

where a is the distance of closest approach between ions i and j. This assumption, although valid from a electrostatic point of view, neglects ionic volumes and is only valid for dilute solutions (when the inter-ionic distance is larger than the ion size).

The second assumption states that the number n_i of ions around j is given by

$$n_i = n_i^o exp[-w_{ij}(r)/k_B T], \tag{A.6}$$

where $w_{ij}(r)$ is the potential energy corresponding to the mean force exerted between the ions i and j while k_B is the Boltzmann constant and T corresponds to the temperature. The number n_i^o is effectively the concentration of salt solution, whereas the difference $n - n_i^o$ is the average local excess or deficiency of an ion (cation or anion) at a point where the potential energy is w_{ij}. Hence, the charge distribution can be written as

$$\rho_{ion}(r) = \sum_i e z_i n_i = \sum_i n_i^o z_i exp[-w_{ij}(r)/k_B T]. \tag{A.7}$$

The sum runs over all types of ions i, n_i^o is the concentration of ions i while $ez_i n_i$ is the charge of the ion i. The Boltzmann factor $\beta = 1/k_B T$, is the statistical weight multiplying the ionic concentration to account for mean local electric interactions between ions. Adding the ionic charge density, eq. A.7 to the Poisson eq. A.4 leads to the Poisson-Boltzmann equation (PBE):

$$\nabla \cdot [\varepsilon(r) \nabla \phi(r)] = -4\pi \Big(\rho(r) + \rho_{ion}(r) \Big) \tag{A.8}$$

$$\nabla \cdot [\varepsilon(r) \nabla \phi(r)] = -4\pi \Big(\rho(r) + \sum_i n_i^o z_i exp[-\beta w_{ij}(r)] \Big). \tag{A.9}$$

The factor w_{ij} is replaced by the potential energy of an ion i located at a point where there is a potential ϕ_j due to ion j. This is a mean energy because it corresponds to the force acting between i and j after averaging over $N-2$ other ions in all possible positions. This can be approximated as,

$$w_{ij} \approx z_i e \phi_{j(r)}. \tag{A.10}$$

In case of monovalent ions (charge -1, +1), the exponential term of equation A.9 adopts the form $e^{-x} + e^{x}$ and it can be replaced by $2sinh(x)$,

$$\nabla \cdot [\varepsilon(r)\nabla\phi(r)] = -4\pi\Big(\rho(r) + 8\pi n_i^o sinh[-e\beta\phi(r)]\Big) \tag{A.11}$$

There are no general analytical solutions for the PBE, but if it is assumed that the therm $[-\beta w_{ij}(r)] << 1$ as in the Debye-Hückel theory, then is possible to expand the exponential term in a linear approximation ($e^y = 1 + y$). This means that beside having a low concentration of ions in solution, the monovalent ions are diluted sufficiently to increase the mean distance between ions enough to produce a low potential which correlates with the approximation used in equation A.10.

Expanding the exponential term of eq. A.9,

$$\sum_i n_i^o z_i exp[-e\beta\phi(r)] = \sum_i n_i^o z_i + \sum_i \beta n_i^o {z_i}^2 \phi(r), \tag{A.12}$$

where the first term vanishes because of overall electro neutrality of the ionic solution, eq. A.4. Defining the ionic strength $I(r) = (1/2)\sum_i n_i^o {z_i}^2$ and the inverse Debye length $\kappa(r) = \sqrt{8\pi\beta I(r)}$, we obtained the linearized PBE as,

$$\nabla \cdot [\varepsilon(r)\nabla\phi(r)] = -4\pi\rho(r) + \kappa^2(r)\phi(r). \tag{A.13}$$

The advantage of the linearized PBE is the additivity of the electrostatic potentials that makes applications easier and faster. This equation enables to compute the electrostatic potential of a macromolecule of known structure in solution. For proteins with very complex dielectric boundaries at the protein surfaces, it can be solved only numerically. The most common methods applied in the MEAD (MULTIFLEX) suit of programs [97, 98] and APBS [77, 78], are based on a finite differences.

To apply the finite difference method, all relevant physical quantities (charge q, dielectric constant ε, ionic strength I, electrostatic potential ϕ) are mapped on a grid with constant h, Fig. A.2. The linearized PBE, eq. A.13, is integrated over the volume V of one cubic grid element:

$$\int_V \nabla[\varepsilon(r)\nabla\phi(r)]dr - \int_V 8\pi\beta I(r)\phi(r)dr = \int_V -4\pi\rho(r)dr. \tag{A.14}$$

While the second and third integral are easily resolvable, the first one is more difficult. In a first step, it is transformed into a surface integral using the Gauss theorem:

$$\int_A \varepsilon(r)\nabla\phi(r)dA - 8\pi\beta I_o\phi_o h^3 = -4\pi q_o. \tag{A.15}$$

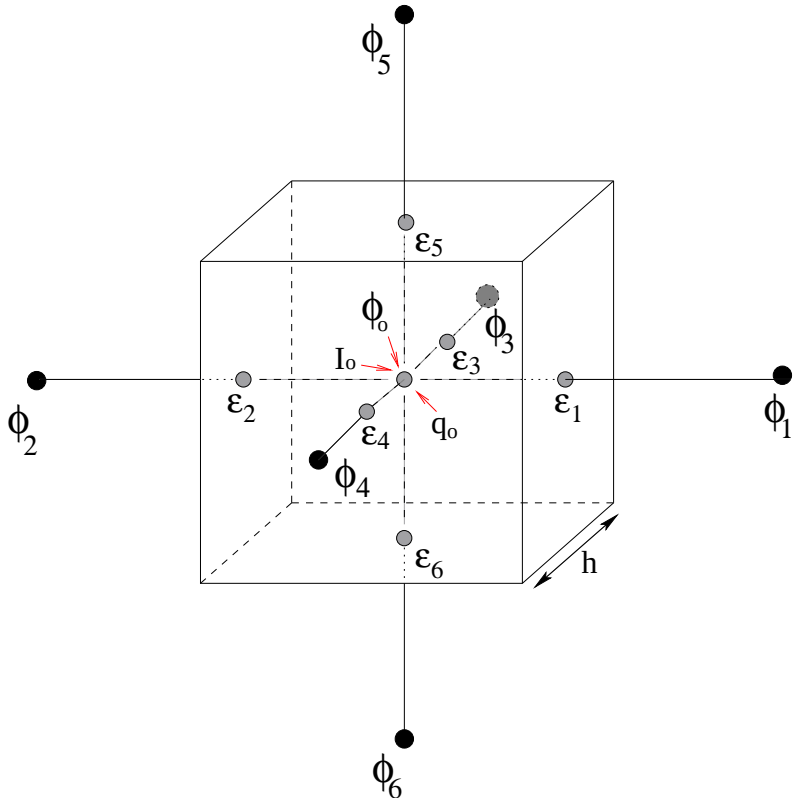

Figure A.2: **Part of the grid used to solve the PBE.**

The surface integral is now calculated separately for all six sides of the cubic grid element. In doing so, the gradient of the electrostatic potential $\nabla\phi$ is substituted by its finite difference form in the respective direction:

$$\sum_{i=1}^{6} = \frac{\varepsilon_i(\phi_i - \phi_o)h^3}{h} - 8\pi\beta I_o\phi_o h^3 = -4\pi q_o. \tag{A.16}$$

Differential operators can now be replaced by differences, resulting in the following finite difference form of the linearized PBE:

$$\phi_o = \frac{\left(\sum_{i=l}^{6}\varepsilon\phi_i\right) + \frac{4\pi q_o}{h}}{\left(\sum_{i=l}^{6}\varepsilon_i\right) + 8\pi\beta I_o h^2}. \tag{A.17}$$

Starting from arbitrary values, the electrostatic potential is calculated iterately for each grid point until a convergence for $\phi(r)$ criteria is met. There is a problem at the borders of the grid, since the grid points at the border have less than six neighbor points. If the grid is much larger than the molecule, so that the border grid points are far away from the charges in the molecule, ϕ outside the grid can be ser to zero.

pK$_a$ and redox potential computations in proteins with a single conformation

The protonation equilibrium of a single titratable group can be described with the Henderson-Hasselbach equation,

$$pH = pK_a + log\frac{[A^-]}{[HA]} \tag{A.18}$$

where HA and A^- are the protonated and deprotonated group. The pK_a value is related to the standard free energy G^o_{prot} of the acid-base equilibrium,

$$G^o_{prot} = -RTln10(pK_a) \tag{A.19}$$

where R is the gas constant ($8.314472 JK^{-1}mol^{-1}$) and T is the absolute temperature in Kelvin. The probability $\langle x \rangle$ that the acid HA is protonated is given by

$$\langle x \rangle = \frac{[HA]}{[HA] + [A^-]}. \tag{A.20}$$

Therefore, the protonation probability of and acid HA is described as

$$\langle x \rangle = \frac{exp\Big[-ln10(pH - pK_a)\Big]}{1 + exp\Big[-ln10(pH - pK_a)\Big]} \tag{A.21}$$

This equation describes the pH dependence of the protonation probability of an acid. Its graphical representation is the sigmoidal curve so called acid-base titration curve. The free energy required to protonate a titratable group at a given pH and temperature is:

$$G_{prot} = RTln10(pH - pK_a) = RTln\left(\frac{\langle x \rangle}{1 - \langle x \rangle}\right) \tag{A.22}$$

The redox-active group and its redox equilibrium can be described similarly. In this case the K_{ET} equilibrium constant is defined as

$$K_{ET} = \frac{[A_{red}]}{[A^+_{oxd}][e^-]} \tag{A.23}$$

In analogy to the Henderson-Hasselbach eq. A.18, one can define the solution re-

dox potential E_{sol} and the standard redox potential (or midpoint potential) E^o, respectively as

$$E_{sol} = -\frac{RT}{F} ln[e^-] \tag{A.24}$$

$$E^o = \frac{RT}{F} lnK_{ET} \tag{A.25}$$

where F is the Faraday constant. Taking the logarithm of eq. A.23, multiplying it by the factor RT/F and using the definitions of eq. A.24 and A.25 one obtains the Nernst law.

$$E_{sol} = E^o + \frac{RT}{F} ln \frac{[A^+_{oxd}]}{[A_{red}]}. \tag{A.26}$$

The standard (^{o}) redox potential E^o of the redox reaction $A^+_{oxd} + e^- \leftrightarrows A_{red}$ in solution is given by

$$E^o = -\frac{\Delta G^o}{n \cdot F} = -\frac{\Delta G^o_{sol} - \Delta G_{SHE}}{n \cdot F}, \tag{A.27}$$

where ΔG^o, ΔG^o_{sol} and ΔG_{SHE} are, respectively, the standard Gibbs free energy of reduction relative to that of H^+ [standard hydrogen electrode (SHE)], the standard Gibbs free energy of reduction, and the Gibbs free energy of the redox reaction $H^+_{water} + e(g) \rightarrow \frac{1}{2} H_{2(g)}$ at SHE. In this study, we only consider electron transfer processes of one electron ($n = 1$).

The probability $\langle x \rangle$ that a redox-active group is in its oxidized state is defined by

$$\langle x \rangle = \frac{[A^+_{oxd}]}{[A^o_{oxd}] + [A_{red}]}. \tag{A.28}$$

While the protonation probability of an acid depends on the solution pH value, the oxidation probability of an isolated redox couple depends on the solution redox potential.

$$\langle x \rangle = \frac{exp\left[\frac{F}{RT}(E_{sol} - E^o)\right]}{1 + exp\left[\frac{F}{RT}(E_{sol} - E^o)\right]}. \tag{A.29}$$

The graphical representation of this equation gives the sigmoidal redox titration curve, where $\langle x \rangle$ is plotted against the solution redox potential E_{sol}. From eq. A.29 one can read that the free energy required to oxidized a redox-active group at a given solution redox potential and temperature is

$$G_{redox} = -F(E_{sol} - E^o) = -RTln \frac{\langle x \rangle}{1 - \langle x \rangle} \tag{A.30}$$

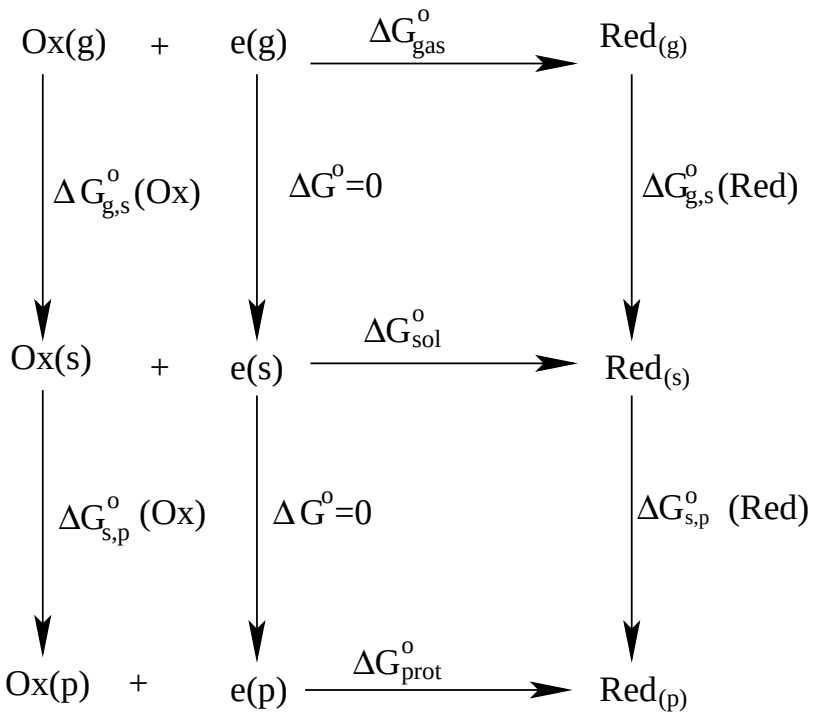

Figure A.3: **Thermodynamic cycle for the redox process to calculate the energy of redox-active groups in solution and in protein from the gas phase properties. The process is given in three media: gas phase (g), aqueous solution (s) and protein (p). The solvation energies to transfer the redox-active group from the gas phase to solution ($\Delta G^o_{g,s}$) and further from solution into protein ($\Delta G^o_{s,p}$) are also shown.**

The pK_a or the E^o value of a titratable group in a protein can be quite different from the value in aqueous solution. To understand the shift of the pK_a/E^o value, one should look at the energetics of the protonation/oxidation equilibrium of that group in different media. The thermodynamic cycle in Fig. A.3 shows the reduction process of a redox-active group in three media: gas phase, water and protein. It also shows the solvation free energy of transferring the oxidized/reduced species from one medium to another. Using the thermodynamic cycle, it is in principle also possible to calculate the oxidation free energy of a redox-active group in a protein if we know the experimental redox free energy value in water or the theoretically calculated value in the gas phase and the energy needed to transfer the redox-active group from solution (gas phase) into the protein.

If there is only a single redox cofactor group in a protein one can obtain the redox potential shift in protein with respect to the redox potential value in aqueous solution E_{sol}, using the thermodynamical cycle of Fig. A.3

$$F \cdot (E_{sol} - E^o) = \Delta G^o_{prot} - \Delta G^o_{sol} = \Delta G^o_{s,p}(Red) - \Delta G^o_{s,p}.(Ox). \qquad (A.31)$$

In a similar way, it is possible to obtain the ΔpK_a shift of a titratable residue in the protein, with respect to the pK_a value in solution

$$pK_a^{prot} - pK_a^{sol} = -\frac{1}{RTln\,10}\left(\Delta G^o_{prot} - \Delta G^o_{sol}\right) = \\ -\frac{1}{RTln\,10}\left(\Delta G^o_{s,prot}(A^-) - \Delta G^o_{s,prot}(AH)\right), \tag{A.32}$$

where A^- and AH are the deprotonated and protonated groups, respectively. In this consideration, we assume that the pK_a and redox potential shifts in a protein are caused by electrostatic interactions between titratable and redox active groups and other charges in the protein and also by a change in the dielectric constant. It is also assumed that the conformation of titratable and redox active groups do not change during the proton/electron transfer. These electrostatic energy differences are obtained by solving the linear PBE were it is necessary to calculate the electrostatic potential for each titratable and redox active group in four different states: protonated (oxidized) and deprotonated (reduced) states in water solution and in the protein for the titratable (redox-active) group.

Protonation and redox potential energies

Due to similarities between protonation and redox reactions, similar expressions can be derived for titratable and for redox-active groups. In the case of titratable groups, the protonation state depends on the solution pH while for redox active groups, the oxidation state depends on the solution redox potential. In the following section we describe, for simplicity, mainly the electrostatic energy of a titratable group inside the protein.

The pK_a in the protein interior is computed by adding a protein induced shift ΔpK_a, which is calculated from electrostatic energies obtained from numerical solutions of the linearized PBE, to the unperturbed (experimental) pK_a, model of the titratable group in solution. Electrostatic energies comprise (i) the desolvation penalty a titratable (or redox active) group has to pay upon entering the protein volume, (ii) the interactions of titratable (redox active) with nontitratable groups as well as (iii) interactions among titratable (and redox active) groups in the protein, which depend on their protonation states. The first two effects give rise to the intrinsic pK_a ($pK_{a,intr}$), that is, the hypothetical pK_a of a titratable group where all other titratable groups in the protein are in their neutral reference protonation state. The latter free energy term is decomposed into individual additive contributions $\Delta\Delta W_{\mu\nu}$ arising from pair wise Coulomb interactions between the titratable residues making it possible to write the total energy of a given protonation microstate n (defined by

$x_\mu^{(n)} \in \{0,1\}$ for all individual titratable residues μ/ν and z_μ that is +1 for acidic and 0 for basic residues including the basic residue his) as [15]

$$\Delta G^{(n)} = \sum_{\mu=1}^{N}\left(x_\mu^{(n)} - z_\mu\right) RTln_{10}\left(pH - pK_{a,intr,\mu}\right) + \sum_{\mu=1}^{N}\left(x_\mu^{(n)} - z_\mu\right)\sum_{\nu=1}^{N}\left(x_\nu^{(n)} - z_\mu\right)\Delta\Delta W_{\mu\nu} \tag{A.33}$$

for a given absolute temperature T and pH. The energy terms $\Delta\Delta W_{\mu\nu}$ are organized in the interaction matrix $\Delta\Delta W$ and contribute to the total energy, equation A.33, only if the considered pair of residues (μ and ν) is in the charged non-reference protonation state. For the calculation of the pK_a of a titratable group μ the full pH titration curve of that residue is derived from repeated evaluation of the thermodynamic average

$$\langle x_\mu \rangle = \frac{1}{Z}\sum_{n=1}^{2^N} x_\mu^{(n)} exp\left(\frac{-\Delta G^{(n)}}{RT}\right), \tag{A.34}$$

where

$$Z = \sum_{n=1}^{2^N} exp\left(\frac{-\Delta G^{(n)}}{RT}\right) \tag{A.35}$$

giving the mean protonation probability of residue at a given temperature T and pH. The sums in equation A.34 were approximated by a Metropolis Monte Carlo (MC) procedure implemented in the software Karlsberg [26].

Redox adapted conformations in proteins

This approach uses a description of conformational flexibility in proteins in terms of redox adapted conformations (RACs) of the protein in the same spirit as pH adapted conformations (PACs) described in detailed by Kieseritzky & Knapp [24]. In the original procedure, the protein conformations are generated by optimizing at a given pH value simultaneously the most probable protonation microstates with the most suitable side chain conformers and H-bond pattern. In the method for generating RACs, the protein conformations are optimized at a given external redox potential simultaneously with the most probable redox state of the cofactor and suitable with side chain conformers and H-bond pattern. The number of protein conformations is small, say 5-20 depending on the protein and the accuracy, which should be achieved. In this approach, equation A.33 has a simple extension:

$$\Delta G^{(n,l)} = \sum_{\mu=1}^{N}\left(x_{\mu}^{(n,l)} - z_{\mu}\right) RTln_{10}\left(pH - pK_{a,intr,\mu}^{(l)}\right) + \sum_{\mu=1}^{N}\left(x_{\mu}^{(n,l)} - z_{\mu}\right)\sum_{\nu=1}^{N}\left(x_{\nu}^{(n,l)} - z_{\mu}\right)\Delta\Delta W_{\mu\nu}^{(l)} + \Delta G_{conf}^{(l)} \tag{A.36}$$

where, l denotes the protein conformation and n the current protonation micro-state. Each conformation (l) is characterized by a separate set of energy look-up tables for $pK_{a,intr}^{l}$ and $\Delta\Delta W^{(l)}$ as well as a specific energy difference $\Delta G_{conf}^{(l)} - G_{conf}^{(ref)}$ between conformation l and an arbitrary reference conformation "ref", which is taken for the charge neutral reference protonation microstate.

While the energy look-up tables $pK_{a,intr}^{(l)}$ and $\Delta\Delta W^{(l)}$ describe the energetics of protonation change within each individual conformation, $G_{conf}^{(l)}$ involves the terms describing the energetics of conformational changes. The calculation of $pK_{a,intr}^{(l)}$ values and the elements of $\Delta\Delta W^{(l)}$ is analogous to the procedure for a single conformer. To avoid arbitrary influences of bonded energies and the van der Waals energies, which can change significantly with small variations in atomic coordinates, $G_{conf}^{(l)}$ included only electrostatic energy contributions (Coulomb and solvation energy).

The electrostatic energy terms are organized in multiple look-up tables to evaluate total energies of protonation pattern and conformations with an MC procedure to compute protonation probabilities for all titratable groups and, furthermore, to select the appropriate conformations for different external redox potential values. These probabilities represent thermodynamic averages, which simultaneously consider different protonation states and protein conformations. Thus, we have included the effect of protein reorganization explicitly.

Generation of RACs

The workflow is depicted in Figure A.4. Initial hydrogen positions were generated using the HBUILD facility in CHARMM [80] and refined by conjugated-gradient energy minimization using standard protonation, that is, acids deprotonated and bases including histidine protonated with $\varepsilon = 1$. At this point, the protonation pattern is computed for the first time with $\varepsilon = 80$ everywhere to weaken the bias of crystal structures for pH 7. All subsequent computations of the protonation pattern are performed with an inhomogeneous dielectric with protein $\varepsilon = 4$ and solvent $\varepsilon = 80$. To generate appropriate redox-adapted conformations (RACs) we started with a simple random search for alternative side chain conformers of residues in salt bridge geometries, which were first individually geometry optimized (with $\varepsilon = 1$ and constrained to crystal structure coordinates). These local conformers were then

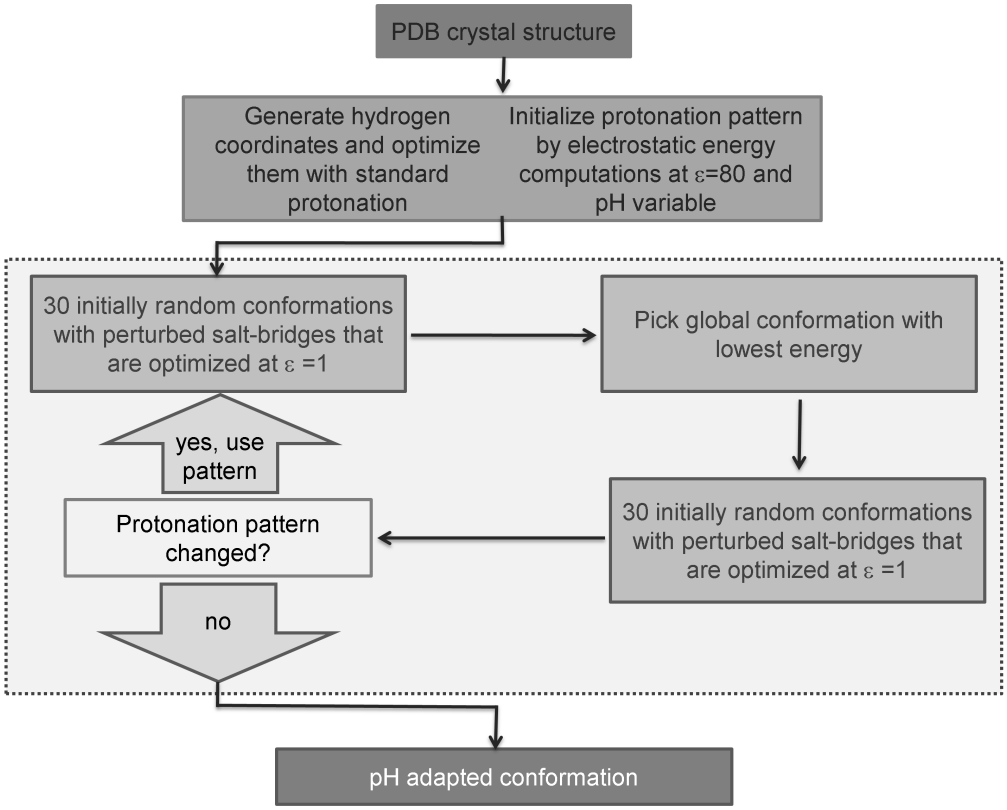

Figure A.4: **Workflow of the procedure to generate pH adapted conformations (PACs) adapted from [24]. In the procedure to generate redox adapted conformation (RACs), a similar spirit was followed with the difference that instead of varying the pH, the RACs are obtained at pH 7 and variable solution redox potential.**

merged in a single global conformation and again geometry optimized (also with $\varepsilon = 1$ and constrained to crystal structure coordinates). To determine the most probable protonation state for the current protein conformation at a given redox state electrostatic energy computations were performed. Then, in consecutive steps the random search of side chain conformers of residues in salt-bridge geometries, geometry optimization ($\varepsilon = 1$ everywhere) with the current protonation pattern and electrostatic energy computations to determine a new protonation pattern were repeated iteratively until the protonation pattern is converged resulting in a redox adapted, self-consistent protein conformation (RAC). We applied a similar method in the past to generate relaxed protein conformations for the study of protonation and redox reactions in the bacterial reaction center [17]. However, the current protocol differs in a special treatment of salt bridges while all other residues are left invariant.

Electrostatic energy computations

The protein is described as a set of discrete partial charges in a dielectric continuum with protein $\varepsilon_p = 4$ inside and solvent $\varepsilon_w = 80$ outside of the protein with ionic strength 100 mM. The boundary between protein and solvent is defined by the solvent accessible surface area of the protein probed by a sphere of 1.4 Å radius. The atomic partial charges in the protein are all considered in detail and are identical to the charges in the CHARMM22 parameter set [81] where available. For the numerical solution of the linearized PBE we employed APBS 0.4 [78]. For the calculation of energy look-up tables, we used TAPBS, which efficiently and conveniently integrates APBS to prepare the necessary input for an MC titration as implemented in the latest version 2.0 of Karlsberg [26]. TAPBS uses directly the three-dimensional structure of the protein and a list of titratable residues. Both Karlsberg 2.0 and TAPBS are available on our group's web site or can be used through the web interface on http://agknapp.chemie.fu-berlin.de/karlsberg that automates the PACs approach.

Appendix B

Redox potentials and quantum chemical computations

Around one-third of all proteins and enzymes require metal ions as cofactors for biological function [31]. The importance of transition metals in biological processes lies on their ability to exist in more than one oxidation states. Therefore, characterization of the redox properties of metals in model complexes is relevant to understand electron transfer reactions and the mechanism of their catalytic action in biochemical processes. In the following section, we present a short description of the method developed by Galstyan and Knapp [28] to compute *ab initio* redox potentials of transition metal complexes. The method is based on the B4(XQ3)LYP approach [28] which employs density functional theory (DFT) and electrostatics.

The B4(XQ3)LYP approach

The B4(XQ3)LYP approach[28] employs the DFT method with a modified functional combined with a post-Hartree-Fock charge dependent empirical correction and subsequent optimized electrostatics to compute solvation energies. In the B4(XQ3)LYP approach, we computed the free energy difference of reduced minus oxidized state in vacuum ΔG_g^o, combining the quantum chemical DFT-based ($G_g^{o,\mathrm{B4}LYP}$) and empirical (G_x) contributions as follows:

$$\Delta G_g^o = \Delta E_o^{\mathrm{B4}LYP} + \Delta ZPE + \Delta G_{0\to 298} + \Delta G_X(q_{red}) = \Delta G_g^{o,\mathrm{B4}LYP} + \Delta G_X(q_{red}) \tag{B.1}$$

with the empirical term ΔG_X (in units of $kcal \cdot mol^{-1}$), depending on the total charge q_{red} of the reduced state, where $\Delta G_X(q_{red}) = G_X(q_{red}) + G_X(q_{red}+1)$ and

$$G_X(q) = -0.333q^3 + 1.545q^2 + 21.634q \tag{B.2}$$

The B4LYP functional contains the same terms as the B3LYP but with weights that differ from the exact exchange. The weight parameters for the two exchange terms in the B4LYP functional are decoupled. While the parameter for the local exchange term is reduced from 0.20 to 0.12, and the other parameters are the same as in the B3LYP functional. An empirical correction G_X compensates for the energy deficit caused by the decrease of the exact exchange contribution and is fitted after the DFT computation to reproduce the experimental redox potentials correctly.

The quantum chemical ground-state electronic energies (E_o^{B4LYP}) are computed in vacuum for both the oxidized and reduced states using the incomplete DFT functional B4LYP, while the zero-point vibrational energies for the thermal excited states at $298K$ ($G_{0\to 298}$) are calculated with the standard B3LYP functional.

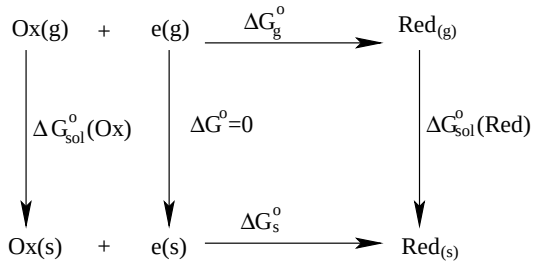

Figure B.1: **Thermodynamic cycle for the redox process.**

The free energy of a redox reaction in solution ΔG_s^o can be calculated routinely using the thermodynamic cycle Fig. B.1, describing the relation between the electron attachment process in vacuum [gas phase (g)] and the corresponding reduction in solution,

$$\Delta G_s^o = \Delta G_g^o + \Delta\Delta G_{sol}^o \tag{B.3}$$

where ΔG_g^o and $\Delta\Delta G_{sol}^o$ are, respectively, the differences of vacuum and solvation energies between the reduced and oxidized states.

The standard (^{o}) redox potential E^o of the redox reaction $Ox{+}e_g \to Red_s$ in solution relative to the absolute potential of the standard hydrogen electrode (SHE), E_{SHE}^o is given by

$$E^o = E_{SHE}^o - \frac{\Delta G_s^o}{nF} \tag{B.4}$$

where $F = 23.06\ kcal \cdot mol^{-1}V^{-1}$ is the Faraday constant and n is the number of transferred electrons (in our case $n = 1$).
For the E_{SHE}^o, the values of 4.43, 4.44 and 4.36 are known. Since the value of the free energy of hydration, included in the calculation of E_{SHE}^o stems from the indirect measurements, their accuracy will influence the value of E_{SHE}^o. The value of $-4.36\ eV$ for E_{SHE}^o has been suggested recently [99], based on the newest results of proton hydration energy from gas-phase experiments. However, the exact value of E_{SHE}^o is not crucial in our method, since the computed redox potentials can be easily adjusted to another value of E_{SHE}^o. Here, we used $-4.44\ V$, as recommended by the IUPAC.

Quantum chemical computations

The quantum chemical computations were done with the DFT method implemented in the program JAGUAR, version 5.5 and version 7.5 [100]. The JAGUAR package was chosen due to its high performance especially for the treatment of systems containing transitions metals. Geometries of all considered model compounds were optimized in vacuum using the B3LYP functional with $LACVP$ effective core potential for the iron atom and the $6-31G^{**}$ basis set for the main group atoms ($LACVP^{**}$). Single-point electronic energies $E_o^{\mathrm{B4}LYP}$ needed for the computation of absolute redox potentials of the model complexes within the B4(XQ3)LYP approach were calculated for optimized geometries using the $LACV3P^{**++}$, including the LACV3P effective core potential for the iron atom and the $6{-}311^{++}G^{**}$ basis set for all other atoms. Vibrational frequency calculations were done using the B3LYP functional with $LACVP^{**}$ basis set without rescaling of vibrational frequencies.

Computation of solvation energy

For the computation of solvation energy ΔG^o_{solv} the solvent was represented as dielectric continuum, with dielectric constants of $\varepsilon_w = 80.0$ and $\varepsilon_{AN} = 37.5$ for water and acetonitrile (AN), respectively. The solvation energies were computed with the program SOLVATE from the MEAD program suite [97, 98] by solving the Poisson equation numerically by a finite difference method. In this approach, the solute is represented by a set of atomic point charges embedded in the solute cavity with dielectric constant $\varepsilon = 1$. Outside the solute cavity, a dielectric constant appropriate for the solvent was taken and the ionic strength was set to zero. The boundaries of the solute are defined by the molecular surface using atomic radii for the solute atoms with solvent probe radii of 1.4 Å, 2.23 Å for water and AN, respectively. The solvent probe radius of AN was estimated by a probe radius calculator implemented in the program JAGUAR, which determines the probe radius according to molecular weight and density of the solvent. Optimized geometries of the solute molecule were used for the computation of solvation energies. The implicit-solvent model in the electrostatic calculations represented by a probe radii and dielectric constant ignores specific properties of the solvent, which in turn influence the solute cavity. To account for these effects in the solvation model different sets of atomic radii for water and AN were used that are the result of optimization performed by Galstyan in a set of model complexes. This are (in Å) for H, C, N, O and S: 1.00, 1.65, 1.60, 1.60 and 1.71 in water and 1.00, 1.80, 1.76, 1.76, 2.18 and 1.76 in AN. The atomic radius of the transition metal does not contribute to the solvation energy, since it is buried by the ligand atoms and its atomic radius is not optimized staying with the value 1.456 Å for Fe from the JAGUAR data set. The two-step focusing procedure was used to solve the Poisson equation on a grid consisting of $(189)^3$ points, using first a low- and then a high resolution grid with lattice constants of 0.4 Å, and 0.1 Å, respectively.

Appendix C

Atomic partial charges

General procedure to compute atomic partial charges

Atomic partial charges were taken from the CHARMM22 force field [80, 81] if available. In case of the iron-sulfur model complexes (ISC) the atomic partial charges were computed quantum chemically. For this purpose a simplified ISC model was geometry optimized in vacuum using DFT with the B3LYP functional in Jaguar [100] at LACVP** level of theory [28]. The electrostatic potential in the neighborhood of this ISC model was computed with the same quantum chemical method and used to calculate the atomic partial charges for the oxidized (Fe^{+3}) and reduced (Fe^{+2}) state with RESP [101, 102]. The atomic partial charges were determined in two stages, using hyperbolic restraints with the total charge fixed. In the first stage of the RESP procedure, the atomic charges were allowed to change with a restraining weight of 0.0005 au. In the second stage, the charges on $C-$ and $H-$ atoms were left free, while all other atomic charges were constrained at their values obtained from the first stage, using a restraining weight of 0.001 au.

Rubredoxin model compound

The simplified ISC model used for Rd consists of $Fe[SC_\beta H_2 C_\alpha H_3]_4$ with C_2 symmetry where the ligand part $[SC_\beta H_2-]$ corresponds to the cysteine side chain and the $[-C_\alpha H_3]$ belongs to the cysteine backbone. The ISC model carries a charge $-1, -2$ in the oxidized and reduced state, respectively. Due to its anionic characteristic, ISC model complexes need to include at least an ethyl group to avoid electronic leakage, but this ISC model is in conflict with the CHARMM[80, 81] force field where the cysteine residue is divided in two molecular segments with neutral charge: backbone and side chain. To introduce the ISC model (conflict free) in the CHARMM force field it is necessary to "remove" the four methyl groups of our model. These four terminal methyl groups of the ISC model carry total charges of $-0.07/-0.11$ and $-0.12/-0.16$ in the oxidized and reduced states, respectively [8]. In the CHARMM force field [80, 81], the charges of the C_α atom and its hydrogen are both positive (+0.07 and +0.09, respectively). To connect the ISC charge model with the CHARMM charge model the total charges of these ISC methyl groups are shifted to the corresponding neighbor C_β atoms of the cysteine side chains and we consider the alchemical model compound $[Fe(SCH_2)_4]^{1-,2-}$ as the appropriate reference model system. Charges are listed in Table C.1 and were published in the Supporting Material of Gamiz-Hernandez *et al* [8].

Table C.1: Atomic partial charges for Rubredoxin (Rd) model compound $[Fe(SCH_2)_4]^{1-,2-}$ with C_2 symmetry, the sum of charges of the methyl group $[CH_3]$ is added to the carbon atom corresponding to C_β of the cysteine side chain. The residue numbering refers to Rd from *Clostridium Pasterianum*, see Fig. 3.1.

residue	atom type	oxidized	reduced
Fe	Fe	0.978	1.084
cys6	SG1	-0.603	-0.797
cys6	CB1	0.344	0.284
cys6	HB11	-0.112	-0.122
cys6	HB12	-0.114	-0.122
cys9	SG2	-0.580	-0.797
cys9	CB2	0.115	0.113
cys9	HB21	-0.049	-0.058
cys9	HB22	0.010	-0.043
cys39	SG3	-0.603	-0.797
cys39	CB3	0.344	0.284
cys39	HB31	-0.112	-0.122
cys39	HB32	-0.114	-0.122
cys42	SG4	-0.580	-0.797
cys42	CB4	0.115	0.113
cys42	HB41	-0.049	-0.058
cys42	HB42	0.010	-0.043

Appendix D

Rubredoxin supporting information

Table D.1: List of considered Rubredoxin crystal structures: wild type (WT) and mutants with available crystal structure: PDB code, author, *pH*, resolution as well as salt-bridges found in the crystal structures. With exception of *Cp* WT (1FHM), *Pf* WT (1CAD) and *Cp* L41A (1SMU) whose crystal structures were solved in the reduced state, all listed structures were crystallized in the oxidized state.

WT/ mutants	crystal structures PDB	author	*pH*	R[b][Å]	salt-bridges[c]		
Clostridium pasterianum (Cp)							
WT	1FHH	[55]	4.6	1.5	-		
	1FHM	[55]	4.6	1.5	D35-K46	E51-K2	
	1IRO	[83]	4.0	1.1	D29-K31	K35-K46	K32-K31
L41A	1SMM	[70]	4.0	1.4	D35-K46		
	1SMU	[70]	4.0	1.4	D35-K46		
V44G[a]	1T9O	[71]	5.0	2.0	D35-K46^{ABC}	D29-K31^{AB}	
V44A[a]	1C09	[53]	4.5	1.6	K35-K46^{ABC}		
V44L	1T9Q	[71]	4.0	1.8	K35-K46	D29-K2	
V44A/G45P[a]	1T9P	[71]		1.5	K35-K46^{ABC}		
Pyrococcus furiosus (Pf)							
WT	1CAA	[84]	8.5	1.8	E49-K6		
	1CAD	[84]	8.5	1.8	E30-K28		
	1BRF	[65]	8.5	1.0	-		
	1VCX	[85]	8.0	1.5	-		
Pyrococcus Abyssi (Pa)							
WT	1YK5	[9]	5.8	1.8	E(T)53-R51^{ABC}	E53-K3^{BCD}	E31-k29^{C}
W4L/R5S[a]	1YK4	[9]	6.0	0.7	E31-K29		
W4L/R5S/A44S[a]	2PYA	[50]	6.0	0.9	E31-K29	E53-K3	D14-K3
Desulfovibrio vulgaris (Dv) Hildenborough strain							
WT	7RXN	[86]		1.5	-		
	8RXN	[87]		1.0	-		
	1RB9	[103]	4.5	0.9	E12-K3		
Desulfovibrio vulgaris (Dv) Miyazaki strain							
WT	1RDV	[88]	7.4	1.9	-		
	2RDV	[88]	7.4	1.9	E12-K3^{AC}	D21^{C}-K2^{A}	D21^{B}-K2^{C}
Desulfovibrio gigas							
WT	1RDG	[89]		1.4	-		
	2DSX	[90]	4.6	0.7	-		
Desulfovibrio desulfuricans (Dd)							
WT	6RXN	[92]		1.5	-		
Pseudomonas aeruginosa (Ps)							
WT	2V3B	[36]	-	2.4	E15-R2	E31-R2	

[a] Solved as trimers (tetramers), labeled A, B, C , (D) accordingly,
[b] R stands for resolution of the crystal structure,
[c] salt-bridges (SB) were calculated with VMD using a minimum distance of 3.2 Å between N and O. We report SB in different monomers (intramolecular) and SB between two monomers (intermolecular). The labels A,B,C indicate the chain of the monomer the salt-bridge is formed. E^{T} refers to the C-terminal acidic group of E54.

Table D.2: Sequence alignment of Rubredoxin *Clostridium Pasterianum* (*Cp*) WT and mutants with available crystal structure. First three lines refer to different WT Rd crystal structures in the oxidized (1IRO and 1FHH) and in the reduced state (1FHM). The others refer to *Cp* mutants, all solved in the oxidized state but one, L41A (1SMU) that was solved in the reduced state. In case the crystal structure was solved as a trimer, we indicate with A, B or C the monomer next to the PDB code in the first column. Highlighted in bold we indicate the mutant residues, while indicated with an arrow the amino acid side chains that present different rotamers with respect to the *Cp* WT 1FHH. The latter was obtained after backbone alignment (Kabsch algorithm) of all structures and visualization with VMD.

```
Cp      1 . . . . . 10. . . . . 20. . . . . 30. . . . . 40. . . . . 50. . . .
1IRO    MKKYTCTVCGYIYNPEDGDPDNGVNPGTDFKDIPDDWVCPLCGVGKDQFEEVEE
1FHH    MKKYTCTVCGYIYNPEDGDPDNGVNPGTDFKDIPDDWVCPLCGVGKDQFEEVEE
1FHM    MKKYTCTVCGYIYNPEDGDPDNGVNPGTDFKDIPDDWVCPLCGVGKDQFEEVEE
1C09-A  MKKYTCTVCGYIYNPEDGDPDNGVNPGTDFKDIPDDWVCPLCGAGKDQFEEVEE
1C09-B  MKKYTCTVCGYIYNPEDGDPDNGVNPGTDFKDIPDDWVCPLCGAGKDQFEEVEE
1C09-C  MKKYTCTVCGYIYNPEDGDPDNGVNPGTDFKDIPDDWVCPLCGAGKDQFEEVEE
1T9O-A  MKKYTCTVCGYIYNPEDGDPDNGVNPGTDFKDIPDDWVCPLCGGGKDQFEEVEE
1T9O-B  MKKYTCTVCGYIYNPEDGDPDNGVNPGTDFKDIPDDWVCPLCGGGKDQFEEVEE
1T9O-C  MKKYTCTVCGYIYNPEDGDPDNGVNPGTDFKDIPDDWVCPLCGGGKDQFEEVEE
1T9Q    MKKYTCTVCGYIYNPEDGDPDNGVNPGTDFKDIPDDWVCPLCGLGKDQFEEVEE
1T9P-A  MKKYTCTVCGYIYNPEDGDPDNGVNPGTDFKDIPDDWVCPLCGAPKDQFEEVEE
1T9P-B  MKKYTCTVCGYIYNPEDGDPDNGVNPGTDFKDIPDDWVCPLCGAPKDQFEEVEE
1T9P-C  MKKYTCTVCGYIYNPEDGDPDNGVNPGTDFKDIPDDWVCPLCGAPKDQFEEVEE
1SMM    MKKYTCTVCGYIYNPEDGDPDNGVNPGTDFKDIPDDWVCPACGVGKDQFEEVEE
1SMU    MKKYTCTVCGYIYNPEDGDPDNGVNPGTDFKDIPDDWVCPACGVGKDQFEEVEE
```

Table D.3: List of measured redox potentials (E^o_{exp}) for rubredoxin (Rd) wild type (WT) and mutants with and without available crystal structure. We also report (if available) pH, temperature and the authors of different measurements.

rubredoxin species	WT/ mutants	E^o_{exp} $[mV]$	pH	temperature ^oC	author
Clostridium pasterianum (Cp)	WT	-74	8.0		[104, 105]
		-77	7.5	25	[67]
		-57	7.0	25	[106]
		-55	7.0		[51, 71]
	L41A	-27	7.6		[70]
	V44G	0	7.5	25	[67]
		+35			[71]
	V44A	-24	7.5	25	[67]
		+31	7.6		[71]
	V44L	-87	7.5	25	[67]
		+61			[71]
	V44G/G45P	+40			[71]
		18			[a]
	V8A	-44			[52]
	V8D	-28			[52]
	V8G	-7			[52]
	V8I	-81			[52]
	V8L	-82			[52]
	V8R	-15			[52]
	V44I	-53			[52]
	V8G/V44G	+39			[52]
	V8I/V44G	-13			[52]
	V8I/V44I	-55			[52]
Pyrococcus furiosus (Pf)	WT	0	8.0	25	[94]
		-40	10.0	25	[94]
		31	6.7	25	[59]
		-93	6.7	95	[59]
Pyrococcus abyssi (Pa)	WT	-18			[9]
	W4L/R5S	-36			[9]
	W4L/R5S/A44S	20			[50]
Desulfovibrio vulgaris Hildenborough strain (*Dv* H)	WT	0	8.6		[53, 107]
Desulfovibrio vulgaris Miyasaki strain (*Dv* M)	WT	+5	7.0		[108]
		-5			
Desulfovibrio gigas (Dg)	WT	+6			[53]
Desulfovibrio desulfuricans (Dd)	WT	+25			[109]
Pseudomonas auruginosa (Ps)	WT	0			[b]

[a] This value was obtained by substracting the difference (22 mV) between measured redox potentials observed between the group of Wedd [67] and Kang [71],

[b] For Rd from *Ps* there is no measured redox potential, nevertheless, it has been suggested that it should be around 0 mV [36].

Salt-bridges found in redox adapted conformations

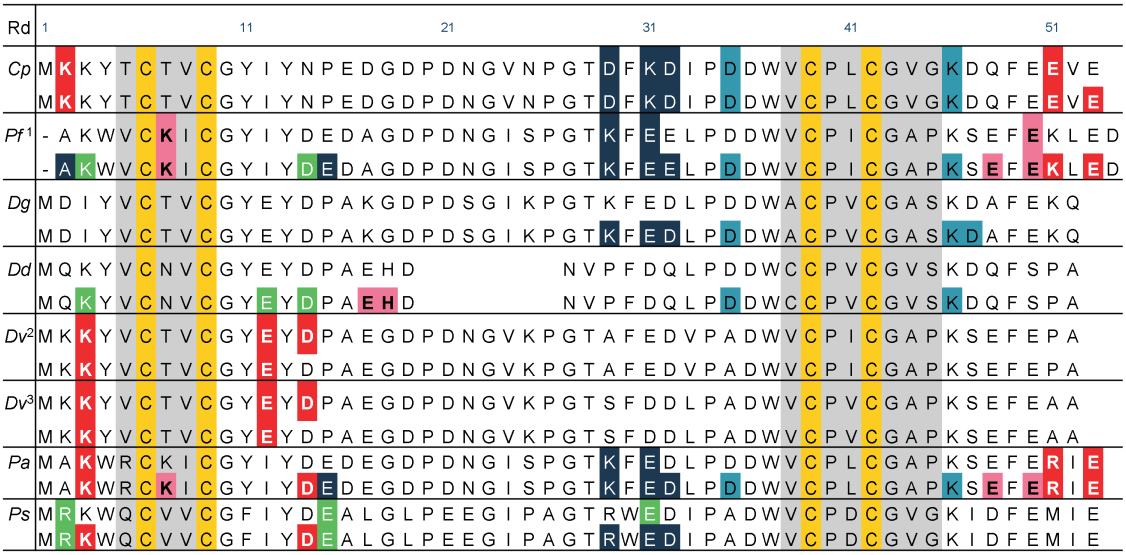

Figure D.1: Rd sequence alignment displaying salt-bridges observed in crystal structures and salt-bridges observed in the most populated RACs (first and second row of each protein, respectively). The numbers in the first line refer to the residues in Rd from *Cp*. Residues surrounding ISC are marked by gray background while cysteine residues of the ISC are marked in yellow. Amino acids involved in the same salt-bridge pattern are marked by the same background color (colors used are dark blue/light blue/red/green/pink). Rd abbreviations refer to: *Clostridium Pasterianum* (*Cp*), *Pyrococcus furiosus* (*Pf*), *Desulfovibrio gigas* (*Dg*), *Desulfovibrio desulfuricans* (*Dd*), *Desulfovibrio vulgaris* (*Dv*) (with two different strains), *Pyrococcus Abyssi* (*Pa*), and *Pseudomonas Aeruginosa* (*Ps*).

Table D.4: Contributions of salt-bridges (SB) to Rd redox potentials for two species, *Pyrococcus furiosus* (*Pf*) and *Clostridium pasteurianum* (*Cp*); E^o_{full} is the computed Rd redox potential using the highest populated RACs of *Cp* (six) and *Pf* (five), while E^o_{zero} is the computed redox potential contribution obtained by setting to zero the atomic partial charges of the side chains of amino acid pairs involved in a salt-bridge including the N-terminal group and if existing in the crystal structure also the C-terminal group.

Pyrococcus furiosus $E^o(full) = +26\ mV$		*Clostridium pasterianum* $E^o(full) = -65\ mV$	
SB pair	$E^o_{full} - E^o_{zero}$ [mV]	SB pair	$E^o_{full} - E^o_{zero}$ [mV]
N-term - E14	1.4	K2-E51	-2.8
K2-D13	2.4	D29-K31	-13.9
K2-D15	1.3	K31-D32	1.6
K6-E47	6.8	K2-E53	2.7
K28-E30	-3.3	D35-K46	-1.5
K28-E31	3.5		
D34-K45	-2.5		
K50-E52	0.8		

Bibliography

[1] J. J. R. Frausto da Silva, R. J. P. Williams, second edition, 2001. 1, 5

[2] G. R. Moore, G. W. Pettigrew, Rogers N. K., "Factors influencing redox potentials of electron transfer proteins" *Proc. Natl. Acad. Sci.*, **83**:4998–4999, 1986. 1

[3] R. Cammack, "Iron-Sulfur Proteins" *Adv. Inorg. Chem.*, **38**, 1992. 2

[4] A. W. Bott, "Redox properties of electron transfer metalloproteins" *Current Separations*, **18**:47–54, 1999. 2

[5] P. J. Stephens, D. R. Jollie, A. Warshel, "Protein control of redox potentials of iron-sulfur proteins" *Chem. Rev.*, **96**:2491–2531, 1996. 2, 13, 14, 21, 26

[6] L. M. Hunsicker-Wang, A. Heine, Y. Chen, E. P. Luna, T. Todaro, J. A. Fee, "High-Resolution Structure of the Soluble, Respiratory-Type Rieske Protein from Thermus Thermophilus: analysis and comparison" *Biochemistry*, **42**:7303–7317, 2003. 3, 12, 13

[7] E. I. Solomon, X. Xie, A. Dey, "Mixed valent sites in biological electron transfer" *Chem. Soc. Rev.*, **37**:623–638, 2008. 13

[8] A. P. Gamiz-Hernandez, A. S. Galstyan, E. W. Knapp, "Understanding Rubredoxin Redox Potentials: Role of H-bonds on Model Complexes" *J. Chem. Theory Comput.*, **5**:2898–2908, 2009. 2, 3, 4, 12, 13, 14, 15, 26, 29, 51

[9] H. Bonisch, C. L. Schmidt, P. Bianco, R. Ladenstein, "Ultrahigh-resolution study on pyrococcus abyssi rubredoxin I 0.69 A x-ray structure of mutant w4l/r5s" *Acta crystallogr. D*, **61**:990, 2005. 3, 18, 19, 21, 23, 54, 56

[10] S. Iwata, M. Saynovits, T. A. Link, Hartmul M., "Structure of a water soluble fragment of the "Rieske" iron-sulfur protein of the bovine heart mitochondrial cytochrome bc_1 complex determined by MAD phasing at 1.5 Åresolution." *Structure*, **4**:567–579, 1996. 6

[11] A. P. Gamiz-Hernandez, G. Kieserisky, A. S. Galstyan, E. W. Knapp, "Understanding Properties of Cofactors in Proteins: Redox Potentials of Synthetic Cytochromes b" *ChemPhysChem*, **11**:1196–2006, 2010. 5, 10, 14, 32

[12] H. K. Rau, N. De Jonge, W. Haehnel, "Combinatorial Synthesis of Four-Helix Bundle Hemoproteins for Tuning of Cofactor Properties" *Angew. Chem. Int. Ed*, **39**:250–253, 2000. 5, 32

[13] A. Warshel, S. Russell, "Calculations on electrostatic interactions in biological systems and in solutions" *Quarterly Review of Biophysics*, **17**:283–422, 1984. 6, 7, 33

[14] A. Warshel, A. Papazyan, "Electrostatic effects in macromolecules: fundamental concepts and practical modeling" *Curr. Opin. Struc. Biol.*, **8**:211–217, 1998. 7, 33

[15] G. M. Ullmann, E. W. Knapp, "Electrostatic models for computing protonation and redox equilibria in proteins" *Eur. Biophys. J.*, **28**:533–551, 1999. 7, 14, 33, 42

[16] A. Warshel, P. K. Sharma, M. Kato, W. W. Parson, "Modeling electrostatic effects in proteins" *Biochim. Biophys. Acta*, 1647–1676. 6, 33

[17] B. Rabenstein, G. M. Ullmann, E. W. Knapp, "Calculation of protonation patterns in proteins with structural relaxation and molecular ensembles - application to the photosynthetic reaction center" *Eur. Biophys. J.*, **27**:626–637, 1998. 7, 14, 33, 44

[18] D. M. Popovic, S. D. Zaric, B. Rabenstein, E. W. Knapp, "Artificial cytochrome b: computer modeling and evaluation of redox potentials" *J. Am. Chem. Soc.*, **123**:6040–6053, 2001. 14

[19] P. Voigt, E. W. Knapp, "Tuning Heme Redox Potentials in the Cytochrome c Subunit of Photosynthetic Reaction Centers" *J. Biol. Chem.*, **278**:51993–52001, 2003. 14

[20] H. Ishikita, G. Morra, E. W. Knapp, "Redox potential of quinones in photosynthetic reaction centers from Rhodobacter sphaeroides: dependence on protonation of Glu-L212 and Asp-L213" *Biochemistry*, **42 (13)**:3882–3892, 2003. 14

[21] H. Ishikita, E. W. Knapp, "Variation of Ser-L223 hydrogen bonding with the QB redox state in reaction centers from Rhodobackter sphaeroides" *J. Am. Chem. Soc.*, **126**:8059–8064, 2004.

[22] H. Ishikita, E. W. Knapp, "Redox potential of cytochrome c550 in the cyanobacterium Thermosynechococcus elongatus" *FEBS Lett.*, **579**:3190–3194, 2005. 14

[23] H. Ishikita, W. Saenger, J. Biesiadka, B. Loll, E. W. Knapp, "How photosynthetic reaction centers control oxidation power" *Proc. Natl. Acad. Sci.*, **103**:9855–9860, 2006. 14

[24] G. Kieseritzky, E. W. Knapp, "Optimizing pKA computation in proteins with pH adapted conformations" *Proteins: Structure, Function, and Bioinformatics*, **71**:1335–1348, 2008. 7, 14, 16, 18, 33, 42, 44

[25] A. Warshel, A. Papazyan, I. Muegge, "Microscopic and semimacroscopic redox calculations: what can be and cannot be learned from continuum models" *J. Biol. Inorg. Chem.*, **2**:147–152, 1997. 7

[26] B. Rabenstein, E. W. Knapp, "Calculated pH-dependent population and protonation of carbon-monoxy-myoglobin conformers" *Biophys. J.*, **80**:1141–1150, 2001. 7, 14, 18, 42, 45

[27] G. Kieseritzky, E. W. Knapp, "Improved pKa prediction: combining empirical and semimicroscopic methods" *J. Comput. Chem.*, **29 (15)**:2575–2581, 2008. 7, 14, 16, 18

[28] A. Galstyan, E. W. Knapp, "Accurate redox potential computations of mononuclear Iron, Manganese and Nickel model complexes." *J. Comput. Chem.*, **30**:203–211, 2009. 9, 14, 47, 51

[29] L. E. Maelia, M. Millar, S. A. Koch, "General synthesis of iron(III) tetrathiolate complexes. Structural and spectroscopic models for the [Fe(Cys-S)4] center in oxidized rubredoxin" *Inorg. Chem.*, **31 (22)**:4594–4600, 1992. 9

[30] D. O. Hall, R. Cammack, K. K. Rao, "The iron-sulphur proteins: evolution of a ubiquitous protein from model systems to higher organisms" *Origins Life Evol. Biosphere*, **5**:363–386, 1974. 13

[31] R. H. Holm, P. Kennepohl, E. I. Solomon, "Structural and Functional Analysis of Metal Sites in Biology" *Chem. Rev.*, **96**:2239–2314, 1996. 13, 47

[32] H. Beinert, R. H. Holm, E. Muenck, "Iron-sulfur clusters: nature's modular, multipurpose structures" *Science*, **277**:653, 1997. 13

[33] J. Imsande, "Iron-sulfur clusters: formation, perturbation, and physiological functions" *Plant Physiol. Biochem.*, **37**:87–97, 1999.

[34] H. Beinert, "Iron-sulfur proteins: ancient structures, still full of surprises" *J. Biol. Inorg. Chem.*, **5**:2–15, 2000. 13

[35] J. B. van Belien, M. Neuenschwander, "Rubredoxins Involved in Alkane Oxidation" *J. Bacteriol.*, **184**:1722–1732, 2001. 13

[36] G. Hagelueken, L. Wiehlmann, T. M. Adams, H. Kolmar, D. W. Heinz, B. Tuemmler, W. D. Schuber, "Crystal structure of the electron transfer complex rubredoxin-rubredoxin reductase of Pseudomonas aeruginosa" *Proc. Natl. Acad. Sci.*, **104**:12276–12281, 2007. 13, 18, 54, 56

[37] L. Noodleman, J. G. Norman Jr., J. H. Osborne, A. Aizman, D. A. Case, "Models for ferredoxins: electronic structures of iron-sulfur cluster with one, two and four iron atoms" *J. Am. Chem. Soc.*, **107**:3418–3426, 1985. 13

[38] J. M. Mouesca, J. L. Chen, L. Noodleman, D. Bashford, D. A. Case, "Density functional/Poisson-Boltzmann calculations of redox potentials for iron-sulfur clusters" *J. Am. Chem. Soc.*, **116**:11898–11914, 1994. 13

[39] L. Noodleman, T. Lovell, T. Liu, F. Himo, R. A. Torres, "Insights into properties and energetics of iron-sulfur proteins from simple clusters to nitrogenase" *Curr. Opin. Chem. Biol.*, **6**:259–273, 2002.

[40] R. A. Torres, T. Lovell, L. Noodleman, D. A. Case, "Density Functional and Reduction Potential Calculations of FeS Clusters" *J. Am. Chem. Soc.*, **125**:1923–1936, 2003.

[41] L. Noodleman, W. G. Han, "Structure, redox, pka, spin. A golden tetrad for understanding metalloenzyme energetics and reaction pathways" *J. Biol. Inorg. Chem.*, **11**:674–694, 2006. 13

[42] N. N. Nair, J. Ribas-Arino, V. Staemmler, D. Marx, "Magnetostructural dynamics from Hubbard-U Corrected Spin-Projection: [2Fe2S] Complex in Ferredoxin" *J. Chem. Theory Comput.*, **6**:569–575, 2010. 13

[43] R. Venkateswara, R. H. Holm, "Synthetic analogues of active sites of iron-sulfur proteins" *Chem. Rev.*, **104**:527–259, 2004. 13

[44] Y. Song M. R. Gunner, J. Mao, J. Kim, "Factors influencing the energetics of electron and proton transfers in proteins. What can be learned from calculations?" *Biochimica et Biophysica Acta*, **1757**:942–968, 2006.

[45] A. Dey, F. E. Jenney Jr., M. W. W. Adams, E. Babini, Y. Takahashi, K. Fukuyama, K. O. Hodgson, B. Hedman, E. I. Solomon, "Solvent Tuning of Electrochemical Potentials in the Active Sites of HiPIP Versus Ferredoxin" *Science*, **318**:1464, 2007. 13

[46] E. T. Adman, K. D. Watenpaugh, L. H. Jensen, "NH—S Hydrogen bonds in Peptococcus aerogenes ferredoxin Clostridium Pasteurianum rubredoxin and Chromatium high potential iron protein" *Proc. Natl. Acad. Sci.*, **72**:4854–4858, 1975. 13

[47] I. J. Lin, E. B. Gebel, T. E. Machonkin, W. M. Westler, J. L. Markley, "Correlation between hydrogen bond lengths and reduction potentials in Clostridium pasteurianum rubredoxin" *J. Am. Chem. Soc.*, **125**:1464–1465, 2003. 13

[48] I. J. Lin, E. B. Gebel, T. E. Machonkin, W. M. Westler, J. L. Markley, "Changes in hydrogen-bond strengths explain reduction potentials in 10 rubredoxin variants" *Proc. Natl. Acad. Sci.*, **102**:14581–14586, 2005. 13

[49] E. I. Solomon, S. I. Gorelsky, A. Dey, "Metal-thiolate bonds in bioinorganic chemistry" *J. Comput. Chem.*, **27**:1415–1428, 2006.

[50] H. Boenisch, C. L. Schmidt, P. Bianco, R. Ladenstein, "Ultrahigh-resolution study on Pyrococcus abyssi rubredoxin: II. Introduction of an O-H...S-Fe hydrogen bond increase the reduction potential by 65 mV" *J. Biol. Inorg. Chem.*, **12**:1163–1171, 2007. 13, 18, 19, 23, 29, 54, 56

[51] Q. Zeng, E. T. Smith, D. M. Kurtz Jr., R. A. Scott, "Protein determinants of metal site reduction potentials: site-directed mutagenesis studies of Cp rubredoxin" *Inorg. Chim. Acta*, **242**:245–251, 1996. 13, 14, 56

[52] H. Zheng, S. J. Kellog, A. E. Erickson, N. A. Dubauskie, E. T. Smith, "Redox properties of rubredoxin variants as a function of solvent composition and temperature: investigation of monopolar and dipolar interactions" *J. Biol. Inorg. Chem.*, **8**:12–18, 2003. 13, 14, 26, 56

[53] M. K. Eidsness, A. E. Burden, K. A. Richie, D. M. Kurtz, R. A. Scott, E. T. Smith, T. Ichiye, B. Beard, T. Min, C. Kang, "Modulation of the redox potential of the [Fe(SCys)(4)] site in rubredoxin by the orientation of a peptide dipole" *Biochemistry*, **38**:14803, 1999. 13, 18, 26, 54, 56

[54] P. Kennepohl, E. I. Solomon, "Electronic structure contributions to electron-transfer reactivity in iron-sulfur active sites: 2. Reduction potentials" *Inorg. Chem.*, **42**:689–695, 2003. 13

[55] T. Min, C. E. Ergenekan, M. K. Eidsness, T. Ichiye, C. Kang, "Leucine 41 is a gate for water entry in the reduction of Clostridium pasteurianum" *Protein Sci.*, **10**:613, 2001. 13, 14, 18, 24, 26, 54

[56] M. Millar, J. F. Lee, T. O'Sullivan, S. A. Koch, R. Fikar, "Models for the iron-sulfur protein rubredoxin: the use of sterically hindered thiolate ligands to stabilize [Fe(SR)4]1- complexes; some considerations of the structure [Fe(S-Cys)4] centers in oxidized rubredoxins" *Inorg. Chim. Acta*, **243**:333–343, 1996. 13, 15

[57] G. M. Ullmann, L. Noodleman, D. A. Case, "Density functional calculation of pKa values and redox potentials in the bovine Rieske iron-sulfur protein" *J. Biol. Inorg. Chem.*, **7**:623–639, 2002. 13

[58] P. E. M. Siegbahn, F. Himo, "Recent developments of the quantum chemical cluster approach for modeling enzyme reactions" *J. Biol. Inorg. Chem. 2009, 14, 643-651.*, **14**:643–651, 2009. 13

[59] L. D. Gilles de Pelichy, E. T. Smith, "Redox properties of mesophilic and hyperthermophilic rubredoxin as a function of presure and temperature" *Biochemistry*, **38**:7874–7880, 1999. 13, 14, 19, 26, 56

[60] Altschul S. F., Gish W., Miller W., Myers E. W., Lipman D. J., "Basic local alignment search tool" *J. Mol. Biol.*, **215 (3)**:403–410, 1990. 14

[61] P. R. Blake, J. B. Park, F. O. Bryant, S. Aono, J. K. Magnuson, E. Eccleston, J. B. Howard, M. F. Summers, M. W. W. Adams, "Determinants of protein hyperthermostability: purification and amino acid sequence of rubredoxin from the hyperthermophilic archaebacterium pyrococcus furiosus and

secondary structure of the zinc adduct by NMR" *Biochemistry*, **30**:10885–10895, 1991. 14

[62] R. B. Yelle, N.-S. Park, T. Ichiye, "Molecular dynamics simulations of rubredoxin from Clostridium Pasterianum: changes in structure and electrostatic potential during redox reactions" *Proteins*, **22**:154–167, 1995. 26

[63] P. D. Swartz, B. W. Beck, T. Ichiye, "Structural origins of redox potentials in Fe-S proteins: electrostatic potentials of crystal structures" *Biophys. J.*, **71**:2958–2969, 1996. 26

[64] T. Lazardis, I. Lee, M. Karplus, "Dynamics and unfolding pathways of a hyperthermophilic and mesophilic rubredoxin" *Protein Sci.*, **6**:2589–2605, 1997.

[65] R. Bau, D. C. Rees, D. M. Kurtz, R. A. Scott, H. Huang, M. W. Adams, M. K. Eidsness, "Crystal structure of rubredoxin from pyrococcus furiosus at 0.95 A resolution" *J. Biol. Inorg. Chem.*, **3**:484, 1998. 18, 26, 54

[66] I. Bertini, D. M. Kurtz Jr., M. K. Eidsness, G. Liu, C. Luchinat, A. Rosato, R. A. Scott, "Solution structure of reduced Clostridium Pasterianum rubredoxin" *J. Biol. Inorg. Chem.*, **3**:401–410, 1998.

[67] Z. Xiao, M. J. Maher, M. Cross, C. S. Bond, J. M. Guss, A. G. Wedd, "Mutation of the surface valine residues 8 and 44 in the rubredoxin from Clostridium pasteurianum: solvent access versus structural changes as determinants of reversible potential" *J. Biol. Inorg. Chem.*, **5**, 2000. 14, 19, 23, 56

[68] C. M. Bougault, M. K. Eidsness, J. H. Prestegard, "Hydrogen bonds in rubredoxin from mesophilic and hyperthermophilic organisms" *Biochemistry*, **42**:4357–4372, 2003.

[69] E. A. Dolan, R. B. Yelle, B. W. Beck, J. T. Fischer, T. Ichiye, "Protein control of electron transfer rates via polarization: molecular dynamics studies of rubredoxin" *Biophys. J.*, **86**:2030–2036, 2004.

[70] I. Y. Park, B. Youn, J. L. Harley, M. K. Eidsness, E. Smith, T. Ichiye, C. Kang, "The unique hydrogen bonded water in the reduced form of Clostridium pasteurianum rubredoxin and its possible role in electron transfer" *J. Biol. Inorg. Chem.*, **9**:423, 2004. 14, 18, 19, 24, 54, 56

[71] I. Y. Park, M. K. Eidsness, I. J. Lin, E. B. Gebel, B. Youn, J. L. Harley, E. E. Machonkin, R. O. Frederick, J. L. Markley, E. T. Smith, T. Ichiye, C. Kang, "Crystallographic studies of v44 mutants of Clostridium pasteurianum rubredoxin: effects of side-chain on reduction potential" *Proteins*, **57**:618, 2004. 14, 18, 19, 54, 56

[72] M. Sulpizi, S. Raugei, J. V. Vondele, P. Carloni, M. Sprik, "Calculation of redox properties: understanding short and long range effects in rubredoxin" *J. Phys. Chem. B*, **111**:3969–3976, 2007. 14, 21, 26

[73] L. Xiao, B. Honig, "Electrostatic contributions to the stability of hyperthermophilic proteins" *J. Mol. Biol.*, **289**:1435–1444, 1999. 14, 19, 23

[74] C. N. Pace, "Single surface stabilizer" *Nat. Struct. Biol.*, **7**:345–346, 2000.

[75] D. Perl, U. Mueller, U. Heinemann, F. X. Schmid, "Two exposed amino acid residues confer thermostability on a cold shock protein" *Nat. Struct. Biol.*, **7**:380–383, 2000.

[76] S. Basu, S. Sen, "Turning a mesophilic protein into a thermophilic one: a computational approach based on 3d structural features" *J. Chem. Inf. Model.*, **49**:1741–1750, 2009. 14

[77] M. Holst, F. Saied, "Multigrid solution of the Poisson-Boltzmann equation" *J. Comput. Chem.*, **14**:105–113, 1993. 15, 18, 36

[78] N. A. Baker, D. Sept, S. Joseph, M. J. Holst, J. A. McCammon, "Electrostatics of nanosystems: application to microtubules and the ribosome" *Proc. Natl. Acad. Sci.*, **98**:10037–10041, 2001. 15, 18, 36, 45

[79] G. Kieseritzky, O. Demir-Kavuk, E. W. Knapp, "Karlsberg+ web project" *http://agknapp.chemie.fu-berlin.de/karlsberg/*, 2007. 16

[80] B. R. Brooks, R. E. Bruccoleri, B. D. Olafson, D. J. States, S. Swaminathan, M. Karplus, "CHARMM: A program for macromolecular energy, minimization, and dynamics calculations" *J. Comput. Chem.*, **4**:187–217, 1983. 16, 18, 43, 51

[81] A. D. MacKerell, D. Bashford, Bellott, R. L. Dunbrack, J. D. Evanseck, M. J. Field, S. Fischer, J. Gao, H. Guo, S. Ha, D. Joseph-McCarthy, L. Kuchnir, K. Kuczera, F. T. K. Lau, C. Mattos, S. Michnick, T. Ngo, D. T. Nguyen, B. Prodhom, W. E. Reiher, B. Roux, M. Schlenkrich, J. C. Smith, R. Stote, J. Straub, M. Watanabe, J. Wiorkiewicz-Kuczera, D. Yin, M. Karplus, "All-Atom Empirical Potential for Molecular Modeling and Dynamics Studies of Proteins using the CHARMM22 force field" *J. Phys. Chem. B*, **102**:3586–3616, 1998. 16, 18, 45, 51

[82] K. D. Watenpaugh, L. C. Sieker, L. H. Jensen, "Crystallographic refinement of rubredoxin at 1.2 angstroms resolution" *J. Mol. Biol.*, **138**:615, 1980. 18, 19

[83] Z. Dauter, Wilson K. S., Sieker L. C., J.-M. Moulis, J. Meyer, "Zn and Fe-rubredoxins from Clostridium pasteurianum at atomic resolution: the first high precision model of ZnS4 unit in a protein" *Proc. Natl. Acad. Sci.*, **93**:8836, 1996. 18, 54

[84] M. W. Day, B. T. Hsu, L. Joshuator, J. B. Park, Z. H. Zhou, M. W. Adams, D. C. Rees, "X-ray crystal structures of the oxidized and reduced forms of the

rubredoxin from the marine hyperthermophilic archaebacterium pyrococcus furiosus." *Protein Sci.*, **1**:1494, 1992. 18, 26, 54

[85] T. Chatake M. W. W. Adams E. J. Jr N. Moiseeva R. Bau K. Kurihara, I. Tanaka, N. Niimura, "Neutron crystallographic study on rubredoxin from pyrococcus furiosus by bix-3, a single crystal diffractometer for biomacromolecules" *Proc. Natl. Acad. Sci.*, **2004**:11215, 2004. 18, 54

[86] E. T. Adman, L. C. Sieker, L. H. Jensen, "Structure of rubredoxin from desulfovibrio vulgaris at 1.5 angstroms resolution" *J. Mol. Biol.*, **217**:337, 1991. 18, 54

[87] Z. Dauter, L. C. Sieker, K. S. Wilson, "Refinement of rubredoxin from desulfovibrio vulgaris at 1.0 angstroms with and without restraints" *Acta crystallogr.*, **48**:42, 1992. 54

[88] S. Misaki, Y. Morimoto, M. Ogata, T. Yagi, Y. Higuchi, N. Yasuoka, "Structure determination of rubredoxin from desulfovibrio vulgaris Miyazaki F in two crystal forms." *Acta crystallogr. D*, **55**:408–413, 1999. 18, 54

[89] M. Frey, L. Sieker, F. Payan, R. Haser, M. Bruschi, G. Pepe, J. l. gall, "Rubredoxin from desulfovibrio gigas. A molecular model of the oxidized form at 1.4 angstroms resolution." *J. Mol. Biol.*, **197**:525, 1987. 18, 54

[90] C. J. Chen, Y. H. Lin, Y. C. Huang, M. Y. Liu, "Crystal structure of rubredoxin from desulfovibrio gigas to ultra-high 0.68 angstroms resolution." *Biochem. Biophys. Res. Commun*, **349**, 2006. 18, 54

[91] L. C. Sieker, R. E. Stenkamp, L. H. Jensen, B. Prickril, J. LeGall, "Structure of rubredoxin from the bacterium Desulfovibrio desulfuricans" *FEBS Lett.*, **208**:73–76, 1986. 18

[92] R. E. Stenkamp, L. C. Sieker, L. H. Jensen, "The structure of rubredoxin from desulfovibrio desulfuricans stran 27774 at 1.5 angstroms resolution" *Proteins*, **8**:352–264, 1990. 18, 54

[93] W. Kabsch, "A solution of the best rotation to relate two sets of vectors" *Acta Crystallogr. A*, **32**:922–923, 1976. 19

[94] M. W. Adams, "Novel iron-sulfur centers in metalloenzymes and redox proteins from extremely thermophilic bacteria" *Adv. Inorg. Chem.*, **38**:341–396, 1992. 19, 56

[95] P. D. Swartz, T. Ichiye, "Temperature dependence of the redox potential of rubredoxin from Pyrococcus furiosus: a molecular dynamics study" *Biochemistry*, **35**:13772–13779, 1996. 26

[96] A. Warshel, 2001, "What are the dielectric constants of proteins and how to validate electrostatic models?" *Proteins: Structure, Function and Bioinformatics*, **44**:400–417, 2001. 33

[97] D. Bashford, K. Gerwert, "Electrostatic calculations of the pKa values of ionizable groups in bacteriorhodopsin" *J. Mol. Chem. B*, **303**:22–37, 1992. 36, 49

[98] D. Bashford, *An object-oriented programming suite for electrostatic effects in biological molecules*, volume 1343, 1997. 36, 49

[99] D. L. Lewis, "Reaction to Why Do We Teach Equilibrium Calculations?" *J. Chem. Educ.*, **81 (9)**:1265, 2004. 48

[100] L. L. C. Schroedinger, "Jaguar Computer Program Version: 5.5" 1991-2003. 49, 51

[101] C. Bayly, P. Cieplak, W. Cornell, P. Kollman, "A Well-Behaved Electrostatic Potential Based Method Using Charge Restraints For Determining Atom-Centered Charges: The RESP Model" *J. Phys. Chem.*, **97**:10269–10280, 1993. 51

[102] W. Cornell, P. Cieplak, C. Bayly, P. Kollman, "Application of RESP Charges to Calculate Conformational Energies, Hydrogen Bond Energies, and Free Energies of Solvation" *J. Am. Chem. Soc.*, **115**:9620–9631, 1993. 51

[103] Z. Dauter, S. Butterworth, L. C. Sieker, K. S. Wilson, "Rubredoxin from desulfovibrio vulgaris refined anisotropically at 0.92 angstroms resolution" *PDB ID: 1RB9*, 1999. 54

[104] F. A. Armstrong, H. A. O. Hill, B. N. Oliver, N. J. Walton, "Direct electrochemistry of redox proteins at pyrolytic graphite electrodes" *J. Am. Chem. Soc.*, **106**:921–923, 1984. 56

[105] M. Ayhan, Z. Xiao, M. J. Lavery, A. M. Hamer, K. W. Nugent, A. G. Wedd S. D. B. Scrofani, M. Guss, "The Rubredoxin from Clostridium pasteurianum: Mutation of the Conserved Glycine Residues 10 and 43 to Alanine and Valine" *Inorg. Chem.*, **35**:5902–5911, 1996. 56

[106] W. Lovenberg, B. E. Sobel, "Rubredoxin: a new electron transfer protein from Clostridium pasterianum" *Proc. Natl. Acad. Sci.*, **54**:193–199, 1965. 56

[107] J. LeGall, B. C. Prickril, I. Moura, A. V. Xavier, J. J. G. Moura, B. H. Huynh, "Isolation and characterization of ruberythrin, a non heme iron protein from Desulfovibrio vulgaris that contains rubredoxin centers and a hemerythrin-like binuclear iron cluster" *Biochemistry*, **27**:1636–1642, 1988. 56

[108] F. Shimizu, M. Ogata, T. Yagi, S. Wakabayashi, H. Matsubara, "Amino acid sequence and function of rubredoxin from Desulfovibrio vulgaris Miyazaki" *Biochimie*, **71**:1171–1177, 1989. 56

[109] J. LeGall, M. Y. Liu, C. M. Gomes, V. Braga, I. Pacheco, M. Regalla, A. V. Xavier, M. Teixeira, "Characterization of a new rubredoxin isolated from Desulfovibrio desulfuricans 27774: definition of a new family of rubredoxins" *FEBS Letters*, **429**:295–298, 1998. 56

Understanding the redox behavior of transition metal complexes: from molecular models to protein

---

Summary: In this thesis, the electrostatic interactions governing the energetics of electron transfer (ET) processes in two types of proteins with redox-active cofactors were investigated theoretically. For this purpose a combination of density functional and electrostatic theories were applied to elucidate the function of redox-active proteins. Our attention was focused to calculate the energetics of protonation and oxidation processes in these proteins. The results of the theoretical work presented here, are divided into three mutually related parts.

To compute cofactor redox potentials in proteins by electrostatic energy evaluation one needs the redox potential of a corresponding faithful model compound in solution. In case of iron-sulfur compounds such information is generally not available. Hence, there is need for quantum chemical computations of redox potential values of model compounds. Therefore, I started with the computation of "absolute" redox potentials of iron-sulfur model compounds whose experimental measurements are not available. The redox potential values of these model compounds in aqueous solution are necessary as a reference value to compute their redox potential in protein using the difference in solvation energy of the model compound in water and in protein. In the case of iron-sulfur complexes (ISC), there are no appropriate model compounds available in solution that corresponds to the cofactor in protein. These model compounds are negatively charged and difficult to stabilize in aqueous solution. The redox potentials for a series of mono-metallic ISC was computed and their energetics in different dielectric media was compare to elucidate the different effects that shift their redox potentials inside the protein. We found that there are three main factors influencing the redox potentials of the ISC in the protein: the conformation adopted inside the protein (that may differ from the more energetically favorable in isolation), the number and type of hydrogen bonds towards the ISC and the dielectric environment provided by the ISC surrounding amino acids and the solvation accessibility.

In the second part of the project I wanted to compute the ISC redox potential in rubredoxin (Rd). We used the continuum electrostatic approach where the protein is represented as dielectric continuum with low dielectric constant and individual

atomic partial charges, while the solvent is represented with a high dielectric constant without individual charges. The protonation and oxidation probabilities of titratable groups and the cofactor were computed simultaneously by solving the linearized Poisson-Boltzmann equation numerically on a grid with a subsequent Monte Carlo titration of all titratable groups in the protein. The electrostatic energies were computed using a number of specially prepared protein conformers, which were optimized self-consistently for different pHs and solvent redox potentials with a new algorithm (Karlsberg$^+$) that considers different crystal structures and multiple side chain conformers. The close correlation of our computed ISC redox potentials with experimental results allows quantifying the influence of the different factors on the ISC redox potentials in Rubredoxin. One important factor is for instance, the change of conformation of some amino acid side chains upon reduction of the ISC.

Finally, we present results on redox potential computations of 31 artificial cytochrome b (aCb) mutants including one redox-active heme. Since no crystal structures were available for these aCbs, the coordinates were generated from scratch by a modeling procedure. The agreement between calculated and measured redox potentials allows excluding one of two possible conformations, which the heme can adopt. Accordingly, the heme propionates are pointing to the close end of the four-helix bundle rather than to the open end. Molecular dynamics results demonstrate that the modeled aCb structures remain stable during a long term computer simulation, thus validating the modeled structures. Analysis of the dependence of heme redox potential on protein environment shows that the shifts in redox potentials relative to the model systems in water are due to the low-dielectric medium of the protein and the protonation states of the heme propionates.

In this work new methods have been introduced, combining and improving currently used methods that can provide further and deeper insights in the relationship between structure and function of redox-active proteins. Theoretical investigations presented here, can help to better understand experimental results on redox-active proteins. Many of our results are based on informations from crystal structures. However, introducing special ISC model compounds and modeling aCb structures to investigate their redox behavior, can help to gain deeper understanding of how nature controls cofactor redox potentials in proteins.

Keywords: Iron-sulfur complexes · hydrogen bonds · rubredoxin · cytochrome b · heme · continuum electrostatics · Poisson-Boltzmann equation · redox potential

Redoxeigenschaften der Übergangsmetallkomplexe:

Von molekularen Modellen zu Proteinen

Zusammenfassung: In dieser Arbeit wird der Einfluss elektrostatischer Wechselwirkungen auf die Energetik von Elektronentransferprozessen in zwei Proteinen mit sehr verschiedenen redoxaktiven Kofaktoren theoretisch untersucht. Dazu wurde eine Dichtefunktional Theorie (DFT) mit speziellem Funktional mit elektrostatischer Energieberechnung kombiniert, um die Funktion einiger redoxaktiver Proteine aufzuklären. Das Hauptaugenmerk war dabei auf die Berechnung der Energetik von Protonierungs- und Oxidationsprozessen in diesen Proteinen gerichtet. Die in dieser Arbeit präsentierten Ergebnisse sind in drei miteinander in Zusammenhang stehenden Teilen dargestellt.

Um Redoxpotentiale von Kofaktoren in Proteinen mit Hilfe von elektrostatischen Energien zu berechnen, wird das Redoxpotential entsprechender Modellverbindungen benötigt. Im Fall von Eisen-Schwefel-Verbindungen gibt es keine Daten zu realistischen Modelverbindungen. Aus diesem Grund ist es notwendig die Redoxpotentiale dieser Verbindungen mit quantenchemischen Methoden zu berechnen. Deshalb habe ich zunächst "absolute" Redoxpotentiale von Modellverbindungen berechnet, für die keine experimentellen Werte existieren. Die Redoxpotentiale dieser Modellverbindungen in wässriger Lösung werden als Bezugswerte benötigt, um zusammen mit der Differenz der Solvatationsenergien der Modellverbindung in Wasser und im Protein das Redoxpotential im Protein zu berechnen. Im Fall von Eisen-Schwefel-Komplexen (ISC) gibt es keine passenden Modellverbindungen in Lösung, die den Kofaktoren im Protein entsprechen. Die vorhandenen Modellverbindungen dieser Art sind sehr stark negativ geladen und es ist deshalb schwierig sie in wässriger Lösung zu stabilisieren. Die Redoxpotentiale einer Anzahl von Eisen-Schwefel-Komplexen wurden berechnet und ihre Energien in unterschiedlichen Dielektrika wurden verglichen, um die verschiedenen Effekte, die zur Veränderung ihrer Redoxpotentiale im Protein beitragen, zu erklären. Wir fanden heraus, dass es drei Hauptfaktoren gibt, welche die Redoxpotentiale dieser Kofaktoren in Proteinen beeinflussen: Die Konformation, die im Protein angenommen wird (welche von der im isolierten Zustand energetisch bevorzugten abweicht), die Anzahl und Art von Wasserstoffbindungen mit dem Kofaktor und die dielektrische Umgebung des Kofaktors, sowie auch der Kontakt mit dem Lösungsmittel.

Im zweiten Teil des Projekts, wurden die Redoxpotentiale der Eisen-Schwefel-Komplexe in Rubredoxin (Rd) berechnet. Wir verwendeten einen elektrostatischen Ansatz, in dem das Protein durch ein elektrostatisches Kontinuum mit niedriger Dielektrizitätskonstante und den Partialladungen der einzelnen Atome repräsentiert wird, während das Lösungsmittel durch eine hohe Dielektrizitätskonstante und ohne Partialladungen dargestellt wird. Die Wahrscheinlichkeiten für Protonierung und Oxidation der titrierbaren Gruppen und des Kofaktors wurden durch Lösen der linearisierten Poisson-Boltzmann-Gleichung auf einem räumlichen Gitter berechnet. Anschlieβend wurde die Titration dieser Gruppen mittels einer Monte-Carlo-Methode durchgeführt. Die elektrostatischen Energien wurden unter Verwendung einer Anzahl speziell präparierter Proteinkonformationen berechnet. Diese wurden mit Hilfe eines neuen Algorithmus (Karlsberg+) selbstkonsistent für verschiedene pH Werte und Redoxpotentiale des Lösungsmittels unter Berücksichtigung verschiedener Kristallstrukturen und multiplen Seitenkettenkonformeren optimiert. Die enge Korrelation der von uns berechneten Redoxpotentiale mit experimentellen Werten erlaubt es den Einfluss verschiedener Faktoren auf den genauen Wert des Redoxpotentials der Eisen-Schwefel-Komplexe in Rubredoxin zu quantifizieren. Beispielsweise ist die Änderung der Konformation der Seitenketten einiger Aminosäuren bei der Reduktion des ISC ein wichtiger Faktor.

Schlieβlich zeigen wir die Ergebnisse der Berechnung der Redoxpotentiale von 31 künstlichen Cytochrom-b (Cb) Mutanten mit einem redoxaktiven Häm. Da für diese künstlichen Cbs keine Kristallstrukturen vorliegen wurden die Atomkoordinaten mittels einer Modellierungsmethode erzeugt. Die Übereinstimmung zwischen berechneten und gemessenen Redoxpotentialen erlaubt es eine der beiden möglichen Hämkonformationen auszuschlieβen. Dementsprechend sind die Hämpropionate zum geschlossenen Ende des Vier-Helix-Bündels ausgerichtet. Molekulardynamiksimulationen zeigen die Stabilität der modellierten künstlichen Cb-Strukturen und validieren somit das Modellierungsverfahren. Eine Analyse der Abhängigkeiten des Hämredoxpotentials zeigt, dass die Verschiebung des Redoxpotentials gegenüber dem Modellsystem im Wasser durch die niedrige Dielektrizitätskonstante im Protein und die Protonierungszustände der Hämpropionate erklärt wird.

In dieser Arbeit wurden neue Methoden eingeführt, die gegenwärtige Methoden kombinieren und verbessern, welche uns weitergehende und tiefere Einsichten in die Beziehung zwischen Struktur und Funktion von redoxaktiven Proteinen geben können. Die vorgestellten theoretischen Untersuchungen können zu einem besseren Verständnis experimenteller Ergebnisse von redoxaktiven Proteinen beitragen. Viele unserer Ergebnisse basieren auf Informationen aus Kristallstrukturen. Das

Einführen von speziellen Eisen-Schwefel-Modellkomplexen und die Modellierung künstlicher Cbs zur Untersuchung von deren Redoxeigenschaften, kann helfen, die von der Natur eingesetzten Mechanismen zur Kontrolle der Redoxpotentiale von Kofaktoren in Proteinen besser zu verstehen.

Stichwörter: Eisen-Schwefel-Komplexen · Wasserstoffbrücken · Rubredoxin · Cytochrom-b, Häm · Kontinuumselektrostatik · Poisson-Boltzmann-Gleichung · Redoxpotential